

Spatially-optimized finite-difference schemes for numerical dispersion suppression in seismic applications

Edward Caunt

Email: ec815@ic.ac.uk

Supervised by Dr Gerard Gorman and Dr Rhodri Nelson

03/01/19



Department of Earth Science and Engineering
Imperial College London

A report submitted in partial fulfilment of the requirements for the degree of Geophysics MSci at Imperial College London and Associateship of the Royal School of Mines. It is substantially the result of my own work except where explicitly indicated in the text. The report may be freely copied and distributed provided the source is explicitly acknowledged.

This MSci project was conducted between September 2018 and January 2019
The main body of this dissertation has 5498 words

Abstract

Propagation characteristics of a wave are defined by the dispersion relationship, from which the governing partial differential equation (PDE) can be recovered. PDEs are commonly solved numerically using the finite-difference (FD) method, discretizing the field to a regular grid and evaluating derivatives using values at a position and adjacent points. FD stencils are conventionally constructed from truncated Taylor series expansions which, whilst typically providing good approximation of the PDE in the space-time domain, often differ considerably from the original partial differential in the wavenumber-frequency domain where the dispersion relationship is defined. Consequentially, stable, high-order FD schemes may not necessarily result in realistic wave behavior, commonly exhibiting numerical dispersion: lagging high-frequency components as a product of discretization. A method for optimizing FD stencil weightings via constrained minimization to better approximate the partial derivative in the wavenumber domain is proposed, allowing for accurate propagation with coarser grids than would be otherwise possible. This was applied to second derivatives on a standard grid and first derivatives on a staggered grid. To evaluate the efficacy of the method, a pair of numerical simulations were devised to compare spatially-optimized stencils with conventional formulations of equivalent extent. A spatially-optimized formulation of the 1D acoustic wave equation with Dirichlet boundary conditions is presented, evaluating performance at a range of grid spacings, examining the interval between the theoretical maximum grid spacings for the conventional and optimized schemes in finer detail. Deviation from the analytical solution was calculated for both schemes. The optimized scheme was found to offer superior performance for undersampled wavefields with minimum wavelengths of $4.4\Delta x$ or smaller and heavily oversampled wavefields with minimum wavelengths of $9.5\Delta x$ or greater. Staggered-grid first derivative stencils were then applied to the P-SV elastic wave formulation, simulating seismic wave propagation for a two-layer, water-over-rock model. For staggered conventional and optimized schemes of 6th and 4th order respectively, general performance was comparable although the optimized scheme provided slightly improved numerical dispersion suppression, particularly apparent for S-wave phases. Performance benefits of the proposed method for staggered grids appear to increase with stencil extent, and are comparable to more complex existing methods, implying significant benefits for high-order FD schemes typically used for seismic processing.

Contents

1	Introduction	1
1.1	An introduction to finite-difference methods	1
1.2	Numerical dispersion and its suppression	1
2	Methodology	2
2.1	Derivation of stencil coefficients	2
2.2	Dispersion characteristics of finite-difference schemes	4
2.3	Finite difference implementation	7
3	Test case: 1D acoustic wave propagation	7
3.1	Model formulation	7
3.2	Analytical solution	8
3.3	Performance at near-maximum grid spacings	9
3.4	General performance trends	17
4	Test case: 2D elastic wave propagation	20
4.1	Model formulation	20
4.2	Derivation of stencil coefficients	21
4.3	Performance at near-maximum grid spacings	24
5	Discussion	31
5.1	Summary of test cases	31
5.2	Comparative performance and grid spacing	32
5.3	Optimized scheme behavior for oversampled wavefields	33
5.4	Limits to optimization benefits for staggered schemes	35
6	Conclusions, evaluation, and further work	35

1 Introduction

1.1 An introduction to finite-difference methods

Finite-difference (FD) methods for solving partial differential equations (PDEs) form the cornerstone of much of seismic processing, in applications including seismic migration (e.g. Mufti et al., 1996, Yan et al., 2013, Yan and Liu, 2013) and wave modeling (e.g. Virieux, 1986, Tessmer, 2000). FD methods benefit from simple implementation, reduced memory requirements, and small computational cost compared to other numerical methods (Liu and Sen, 2009a); usage is consequentially widespread. FD methods are not limited to simple domains and can accommodate complex boundary conditions (Lele, 1992). For time marching schemes, temporal derivatives are typically evaluated using a 2nd order FD scheme for reasons of effectiveness and stability (Liu and Sen, 2009a). However, this limits modeling accuracy. Smaller temporal and spatial increments offer a straightforward way to counter this, but incur additional operations, increasing run time (Liu and Sen, 2009a). Methods developed to address this without considerably increasing computational expense include high-spatial-order, staggered-grid, and implicit methods.

The degree of Taylor series truncation used in the derivation of an FD scheme is typically used to express its accuracy, with an error term proportional to the dimensional increment raised to the appropriate power. With high-spatial-order schemes, the error in spatial derivatives is reduced, allowing for coarser grid spacings without introduction of large errors, thereby offsetting inherent costs of larger operators (Liu and Sen, 2009a). Practical benefits include reduced memory requirements as wavefields do not require such heavy oversampling (Dablain, 1986). It is trivial to derive high-spatial-order FD schemes of any order (Liu and Sen, 2009a) and their usage in seismic modeling is widespread (e.g. Dablain, 1986, Yan et al., 2014, Liu, 2009). Additionally, stencils of sufficiently high order can be truncated to remove small coefficients without notably compromising accuracy (Liu, 2009), reducing computational cost. High-order stencils are commonly used in conjunction with staggered grids. Introduced for seismic modeling by Madariaga, 1976, staggered-grid methods evaluate derivatives on spatially offset grids, improving precision and stability of the scheme, and have seen widespread use (e.g. Virieux, 1986, Wang et al., 2014, Etemadsaeed et al., 2016). However, instabilities may arise at sharp parameter contrasts: a relatively common occurrence in seismic models (Liu and Sen, 2009a). Improved stability is achievable with implicit schemes, evaluating spatial using function and derivative values at neighboring points along with function value at the current position (e.g. Liu and Sen, 2009b, Lele, 1992).

A stable, high-order FD scheme will adequately approximate the governing PDE for many applications. However, for wave problems this does not guarantee an acceptable solution. Propagation characteristics of a wave are encoded in frequency-wavenumber space as the dispersion relation (Tam and Webb, 1993, Whitham, 1974), from which the governing PDE can be reconstructed. The dispersion relation takes the form of some function of frequency and wavenumber, typically obtained through spatial and temporal Fourier transforms of the governing PDE. This relationship governs group and phase velocities, along with dispersion characteristics of waves propagating within a medium. It is thus apparent a wave may propagate in an unrealistic manner, even if the FD scheme resembles the governing PDE in the time-space domain (Tam and Webb, 1993). This phenomena is a product of the discretization, referred to as numerical dispersion.

1.2 Numerical dispersion and its suppression

Numerical dispersion results in unrealistic or spurious dependence of phase velocity on frequency and propagation direction (occasionally referred to as numerical anisotropy) (Juntunen and Tsiboukis, 2000), arising from wavefield discretization, causing phase velocity to become a function of grid spacing (Kim and Hoefer, 1990, Yang et al., 2003). This causes high-frequency wave components to lag behind the group, whilst directional dependence causes squaring of circular wavefronts, the net effect being significant distortion of the wave profile. This results in greater dispersion than otherwise expected in

dispersive systems, and is particularly egregious in non-dispersive systems. Methods proposed to suppress numerical dispersion include introduction of artificial anisotropy to increase propagation speed of lagging wave components (Juntunen and Tsiboukis, 2000), flux-corrected transport algorithms (Fei and Lerner, 1995), and nearly analytic discrete methods (Yang et al., 2003, Yang et al., 2010).

An alternative approach is to construct an FD scheme such that it has near-identical dispersion characteristics to the PDE which it approximates (e.g. Tam and Webb, 1993). Note that in accordance with Nyquist-Shannon sampling theorem, four grid spacings are required to define a sine wave without ambiguity. Thus the above criteria need only be the case for wave components with wavenumber α such that $\alpha\Delta x \leq \frac{\pi}{2}$ where Δx is grid spacing in the x direction. Thus an FD stencil whose Fourier transform has minimal misfit with that of the original partial derivative within the window $-\frac{\pi}{2} \leq \alpha\Delta x \leq \frac{\pi}{2}$ is desired. Such schemes are referred to as dispersion-relation-preserving (DRP) schemes (Tam and Webb, 1993).

In this work, a 4th order DRP 1D acoustic wave formulation with zero Dirichlet boundary conditions is presented, extending methods of Tam and Webb, 1993. Performance is compared to the conventional scheme of equal extent, evaluated against the analytic solution at a range of grid spacings. In doing so, the efficacy of spatial optimization is assured and the conditions under which it is effective can be determined. Staggered optimized first-derivative stencils are then derived and applied to a 2D elastic wave test case using the P-SV formulation of Virieux, 1986, aiming to demonstrate the versatility and universal benefits of spatial optimization.

2 Methodology

2.1 Derivation of stencil coefficients

Suppose we wish to evaluate the FD approximation of a spatial derivative of the discretized function u at position l on a uniform grid. Stencil extent of M and N nodes from l in the positive and negative directions respectively must be specified. Thus the FD approximation for the second derivative is expressed as

$$\frac{\partial^2 u}{\partial x^2} \approx \frac{1}{(\Delta x)^2} \sum_{j=-N}^M a_j u_{l+j} \quad (1)$$

where a_j is the stencil coefficient at point u_{l+j} .

Values of a_j are normally obtained by taking Taylor series expansions of terms on the right hand side of the equation, weighted to cancel undesired derivatives given a symmetric or antisymmetric stencil. Finite difference stencils derived in this manner will henceforth be referred to as conventional schemes. Such schemes will typically only acceptably approximate the partial derivative in the time-space domain, deviating significantly in frequency-wavenumber space. Alternatively, stencil coefficients can be specified by requiring that the Fourier transform of the stencil closely approximates that of the partial derivative. Resemblance between dispersion relationships of the FD scheme and governing PDE is thereby assured.

Equation (1) is a special case of the following, trivially recoverable by specifying $x = l\Delta x$.

$$\frac{\partial^2 u}{\partial x^2} \approx \frac{1}{(\Delta x)^2} \sum_{j=-N}^M a_j u(x + j\Delta x) \quad (2)$$

Furthermore, the Fourier transform for a function and its inverse are defined as

$$\tilde{u}(\alpha) = \frac{1}{2\pi} \int_{-\infty}^{\infty} u(x) e^{-i\alpha x} dx \quad (3)$$

$$u(x) = \int_{-\infty}^{\infty} \tilde{u}(\alpha) e^{i\alpha x} d\alpha \quad (4)$$

where α represents the wavenumber. Fourier transforming both sides of (2) yields

$$-\alpha^2 \tilde{u}(\alpha) \approx \left(\frac{1}{(\Delta x)^2} \sum_{j=-N}^M a_j e^{i\alpha j \Delta x} \right) \tilde{u}(\alpha) \quad (5)$$

By inspection of (5), it is apparent that the wavenumber of the Fourier transform of the FD stencil can be expressed as

$$\bar{\alpha}^2 = \frac{1}{(\Delta x)^2} \sum_{j=-N}^M a_j e^{i\alpha j \Delta x} \quad (6)$$

It is also apparent that $(\bar{\alpha}\Delta x)^2$ is a function of $\alpha\Delta x$ with period 2π . To achieve minimal misfit between the Fourier transforms of the partial derivative and FD scheme, stencil weighting are chosen such that the integrated error function

$$\begin{aligned} E &= \int_{-\frac{\pi}{2}}^{\frac{\pi}{2}} |(\alpha\Delta x)^2 - (\bar{\alpha}\Delta x)^2|^2 d(\alpha\Delta x) \\ &= \int_{-\frac{\pi}{2}}^{\frac{\pi}{2}} \left| \kappa^2 + \sum_{j=-N}^M a_j e^{ij\kappa} \right|^2 d\kappa \end{aligned} \quad (7)$$

is minimized. The approximation need only be valid for waves with wavelengths greater than $4\Delta x$, corresponding with $|\alpha\Delta x| < \frac{\pi}{2}$. E is minimized when conditions

$$\frac{\partial E}{\partial a_j} = 0; \quad -N \leq j \leq M \quad (8)$$

are met. Note that whilst Tam and Webb, 1993 outlined optimization of first derivatives, error functions for stencil optimization differ extensively with derivative-order and grid, requiring unique analysis for each derivative type.

For asymmetric stencils ($N \neq M$), $\bar{\alpha}$ is complex. Applying such stencils throughout the computational region will typically result in instabilities, with solutions prone to blowup (Tam and Webb, 1993). Consequentially, central-difference stencils are used exclusively within the main body of the computational domain in this work. Boundaries necessitate limited use of asymmetric stencils, although accumulated numerical instability in these regions is minimal and unlikely to cause issues.

This minimization is combined with the truncated Taylor series method to create an optimized FD scheme. Specifying stencil extent as $N = M = 3$ and 4th order accuracy, a symmetric stencil can be formulated from pairs of Taylor series expansions at appropriate points. Values of a_j are constrained, becoming functions of a single coefficient. Using a_1 as our free parameter, we obtain

$$\begin{aligned}
a_0 &= -\frac{4a_1}{3} - \frac{13}{18} \\
a_2 = a_{-2} &= \frac{9}{20} - \frac{2a_1}{5} \\
a_3 = a_{-3} &= \frac{3a_1}{45} - \frac{4}{45}
\end{aligned} \tag{9}$$

Constrained minimization of E via Gauss-Newton or comparable methods, yields weights for all stencil points.
Thus

$$\begin{aligned}
a_0 &= -2.81299833 \\
a_1 = a_{-1} &= 1.56808208 \\
a_2 = a_{-2} &= -0.17723283 \\
a_3 = a_{-3} &= 0.01564992
\end{aligned} \tag{10}$$

are the coefficients obtained for the 4th order second derivative stencil.

2.2 Dispersion characteristics of finite-difference schemes

The relationship between $(\bar{\alpha}\Delta x)^2$ and $\alpha\Delta x$ over the first half period for the above scheme is shown in figure 1, and alongside other FD schemes in figure 2.

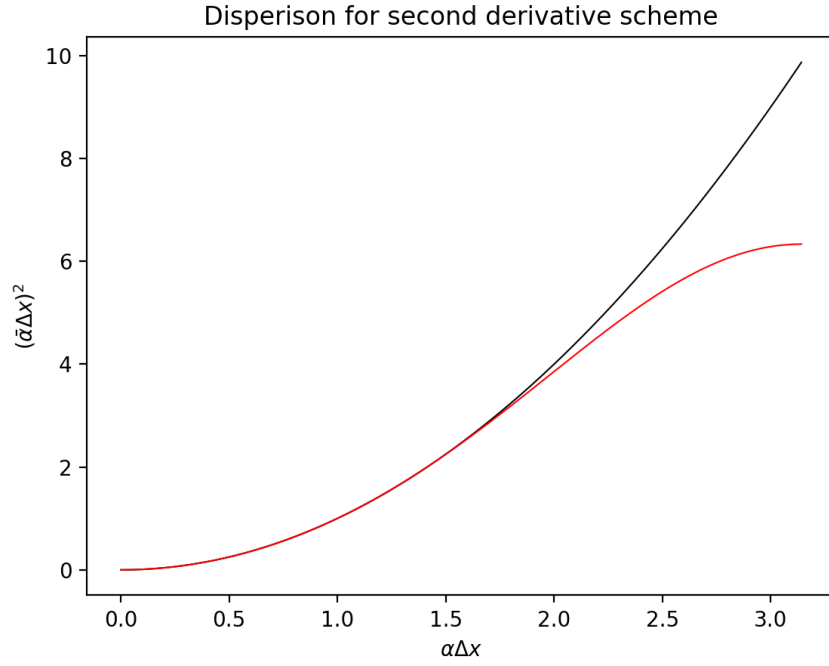


Figure (1) $(\bar{\alpha}\Delta x)^2$ versus $\alpha\Delta x$ for the 4th order optimized central-difference scheme. The solid black line designates the ideal: $(\bar{\alpha}\Delta x)^2 = (\alpha\Delta x)^2$. The curve and ideal are effectively overlaid for $\alpha\Delta x \leq 1.55$, beyond which the two begin to diverge. Therefore the optimized stencil will accurately represent the partial derivative for wavelengths greater than $4.1\Delta x$. Beyond this point, misfit between the ideal and optimized curves increases with larger values of $\alpha\Delta x$. Wave components with wavelengths shorter than $4.1\Delta x$ will not have their propagation characteristics accurately preserved and values beyond the inflection point at $\alpha\Delta x = \pi$ will produce dispersion characteristics that differ considerably from those of the PDE.

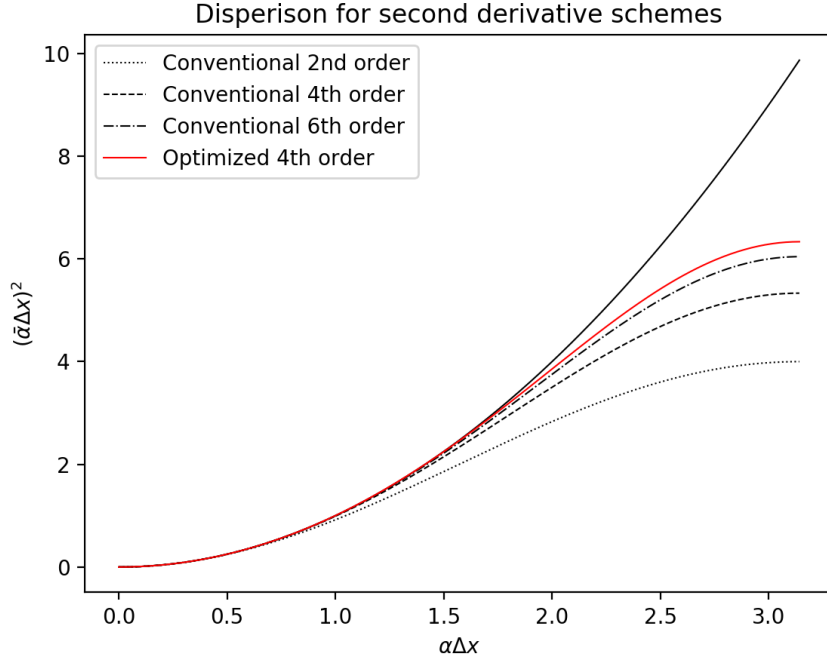


Figure (2) $(\bar{\alpha}\Delta x)^2$ versus $\alpha\Delta x$ for a selection of central-difference schemes. Note the considerable reduction in misfit for the 4th order optimized scheme versus other discretizations. Considering the dispersion curve of the conventional 6th order scheme, it is apparent that deviation from the ideal begins at $\alpha\Delta x = 1.35$, implying adequate approximation only if the shortest wavelength present is greater than $4.7\Delta x$. Thus it can be concluded that a 4th order optimized scheme has greater resolving power than its conventional 6th order counterpart with equal stencil extent ($N = M = 3$). Also shown are dispersion curves for 2nd and 4th order conventional schemes ($N = M = 1$ and $N = M = 2$ respectively). Both schemes deviate from the ideal at much smaller $\alpha\Delta x$: unable to resolve waves with wavelengths smaller than $9.7\Delta x$ and $6.3\Delta x$ respectively, emphasizing the necessity of high-order and optimized schemes for handling high-frequency components.

2.3 Finite difference implementation

Implementation of FD schemes was carried out using Devito, a domain-specific Python module and compiler for FD applications (Luporini et al., 2018). Devito allows for model specification with a handful of high-level symbolic Python objects to build an FD operator, used to generate highly optimized C++ code at runtime via a series of intermediate representations, allowing for complex multi-stage optimizations (Luporini et al., 2018). The generated code is automatically executed, with the solution returned.

Specification of FD stencils is reasonably straightforward, using index notation to access nodes based on their position relative to the central stencil point. Coefficients are specified for each stencil point within the optimized stencil, which can then be used to build the FD operator. By defining “time” and “x” as their respective dimensions, the 4th order accurate spatially-optimized implementation for the 1D acoustic wave equation can be expressed as follows

```
# Optimized stencil coefficients
a_0 = -2.81299833
a_1 = 1.56808208
a_2 = -0.17723283
a_3 = 0.01564992

eq_opt = (a_3*u_opt[time, x - 3]
          + a_2*u_opt[time, x - 2]
          + a_1*u_opt[time, x - 1]
          + a_0*u_opt[time, x]
          + a_1*u_opt[time, x + 1]
          + a_2*u_opt[time, x + 2]
          + a_3*u_opt[time, x + 3])/h_x**2- u_opt.dt2
```

Devito simplifies stencil specification by automatically handling attempts to access out of bounds grid points, negating the need for additional stencils at the boundaries of the computational domain, and can handle a suite of common boundary conditions (Luporini et al., 2018). Applying the FD operator built with this stencil for a specified number of timesteps allows the updated wavefield to be obtained.

Symbolic computation to implement the test cases expedites workflow compared to model building with low-level languages, enabling rapid prototyping in hours as opposed to weeks or months. Performance optimization during compilation results in generated C++ of comparable quality to hand-optimized implementations (Luporini et al., 2018), whilst allowing attention to be focused on the problem at hand. The improved readability of high-level code allows for straightforward transfer from governing PDEs to the computational model. There is presently a dearth of literature using symbolic computation as a tool for implementation DRP schemes, with the method remaining unnoticed as far.

Test cases and example code are located in the supplementary materials.

3 Test case: 1D acoustic wave propagation

3.1 Model formulation

To evaluate the effectiveness of the 4th order spatially-optimized 2nd derivative, a 1D acoustic wave problem was formulated and solved using optimized and conventional stencils. The 1D acoustic wave equation has the form

$$\frac{\partial^2 u}{\partial t^2} = c_0^2 \frac{\partial^2 u}{\partial x^2} \quad (11)$$

where c_0 is the wavespeed. Solutions consist of superpositioned wavetrains of the form

$$u(x, t) = Ae^{i\alpha x - i\omega t} \quad (12)$$

where A represents amplitude and ω is frequency. Inserting this into (11) yields

$$\omega^2 = c_0^2 \alpha^2 \quad (13)$$

This is the dispersion relation for this equation (Whitham, 1974). As the wave will propagate with phase velocity $c = \frac{\omega}{\alpha} = \pm c_0$, it is apparent that the 1D acoustic wave equation is non-dispersive. Any numerical dispersion will thus be particularly obvious.

Straightforward implementation and a simple analytic solution also contributed to the selection of this initial test case. The 1D domain minimized gridpoint count, reducing memory requirements and operations per timestep. Resultant short runtimes enabled rapid debugging and parameter tuning. Zero Dirichlet boundary conditions were applied, recreating the classic “wave on a string” setup, thereby ensuring intuitive behavior, and further simplifying implementation and the analytical solution. Initial displacement was defined as a square wave with amplitude 0.1 and wavelength equal to half the domain length, approximated via Fourier sine series. This ensured obvious numerical dispersion would affect high-frequency components. The series was limited to 100 terms to prevent requirement of an excessively large number of gridpoints to discretize high-frequency wave components without ambiguity, limiting runtime. Initial $\frac{\partial u}{\partial t} = 0$ for all x , again for ease of implementation. A value of $c_0 = 1ms^{-1}$ was selected to simplify the PDE, and domain extent was specified as 10m, producing a standing wave with a period of 5s. A Courant number of 0.2 was empirically determined, achieving acceptable trade-off between accuracy and expediency.

3.2 Analytical solution

As a benchmark for comparison, the system was solved analytically. Consider equation (11): with $c_0 = 1ms^{-1}$, this becomes

$$\frac{\partial^2 u}{\partial t^2} = \frac{\partial^2 u}{\partial x^2} \quad (14)$$

Assuming the solution $u(x, t)$ can be expressed as

$$u(x, t) = T(t)X(x) \quad (15)$$

then via separation of variables, it is straightforward to find that the general solution takes the form

$$u(x, t) = (A \sin(ax) + B \cos(ax)) (C \sin(at) + D \cos(at)) \quad (16)$$

where a, A, B, C, D are constants. Applying the boundary conditions

$$u(0, t) = 0; u(L, t) = 0 \quad (17)$$

where L is domain length yields $B = 0$ and $a = \frac{n\pi}{L}$ for $n \in \mathbb{Z}^+$. Dividing through by A :

$$u(x, t) = \sin\left(\frac{n\pi x}{L}\right) \left(\tilde{C} \sin\left(\frac{n\pi t}{L}\right) + \tilde{D} \cos\left(\frac{n\pi t}{L}\right) \right) \quad (18)$$

Applying the first initial condition

$$u(x, 0) = \sum_{n=1}^{100} b_n \sin\left(\frac{2n\pi x}{L}\right)$$

$$b_n = \frac{4}{L} \int_0^{\frac{L}{2}} f(x) \sin\left(\frac{2n\pi x}{L}\right) dx \quad (19)$$

$$f(x) = \begin{cases} 1, & \text{if } 0 \leq x \leq \frac{L}{4} \text{ or } \frac{L}{2} \leq x \leq \frac{3L}{4} \\ -1, & \text{otherwise} \end{cases}$$

\tilde{D} is found to take the form

$$\tilde{D}_n = \begin{cases} \frac{4}{L} \int_0^{\frac{L}{2}} f(x) \sin\left(\frac{n\pi x}{L}\right) dx, & \text{for all even } n \\ 0, & \text{otherwise} \end{cases} \quad (20)$$

In applying the second initial condition

$$\frac{\partial u}{\partial t}(x, 0) = 0 \quad (21)$$

the particular solution for the PDE is found to be

$$u(x, t) = \sum_{n=1}^{200} \tilde{D}_n \sin\left(\frac{n\pi x}{L}\right) \cos\left(\frac{n\pi t}{L}\right) \quad (22)$$

3.3 Performance at near-maximum grid spacings

From figure 2, the optimized scheme should accurately approximate propagation characteristics of the standing wave for $\Delta x \leq 0.0244\text{m}$, with $\Delta x \leq 0.0213\text{m}$ required for the conventional scheme. Within the region $0.0213\text{m} \leq \Delta x \leq 0.0244\text{m}$ the optimized stencil should yield reduced error; the error of the two schemes converging towards $\Delta x = 0.0213\text{m}$ with similar or superior performance for the conventional scheme thereafter. To verify, both schemes were applied with grid spacings between 0.0200m and 0.0250m , incremented corresponding to addition of 10 gridpoints. The standing wave was propagated over 4 periods (total length 20s) to ensure numerical dispersion error would be apparent at simulation end. Error accumulated by longer simulations resulted in excessively noisy data, limiting propagation

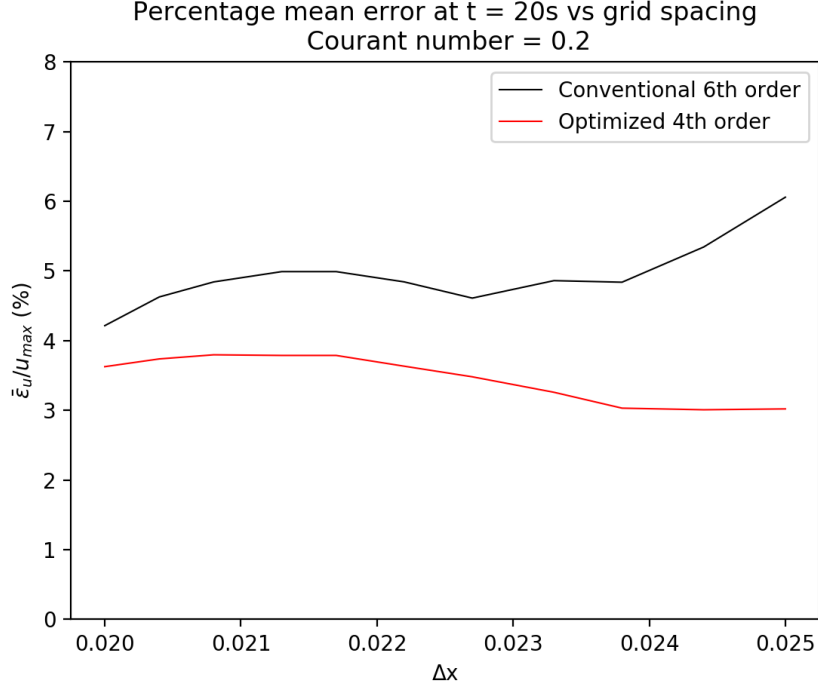
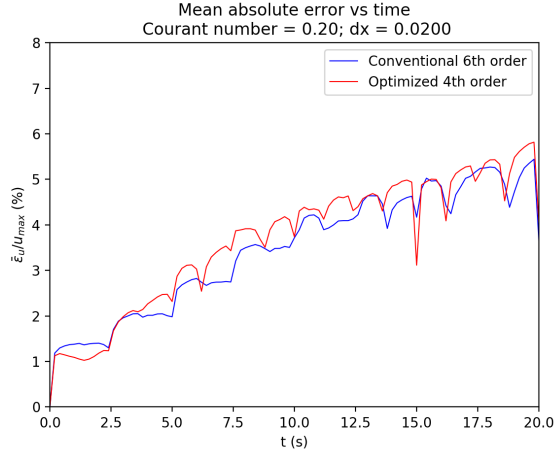


Figure (3) Mean absolute error ($\bar{\epsilon}_u$) evaluated at $t = 20s$, normalized against maximum amplitude versus Δx . Performance for the optimized stencil is considerably better than for the conventional at $\Delta x = 0.0250m$, with $\frac{\bar{\epsilon}_u}{u_{max}} = 3.0\%$ and $\frac{\bar{\epsilon}_u}{u_{max}} = 6.1\%$ respectively. This broadly agrees with the relationship in figure 2: the optimized scheme is expected to offer superior performance in this region. Error for the two schemes converges as expected towards $\Delta x = 0.0213m$. However, the somewhat rough relationship between $\frac{\bar{\epsilon}_u}{u_{max}}$ and Δx throughout the window studied prevents meaningful conclusions based solely upon this data. For adequately small Δx , the conventional scheme should offer equivalent or better performance. Surprisingly, for all Δx within the region of interest, the optimized scheme generates smaller $\bar{\epsilon}_u$: unexpected given the conventional scheme should accurately propagate at the smallest Δx tested. Furthermore, the smallest error for the conventional scheme is greater than the largest error for the optimized within this window. Contrary to expectation, error in the optimized scheme decreases between $\Delta x = 0.0200m$ and $\Delta x = 0.0250m$. Given the Δx interval used, it is unlikely that this reflects small-scale roughness in the relationship between Δx and $\bar{\epsilon}_u$ (although this relationship is seen to be somewhat rough for the conventional scheme). However, it is inconsistent with expected behavior of both truncation and numerical dispersion errors, inferring the presence of some additional factor, possibly concerning the formulation of the test case.

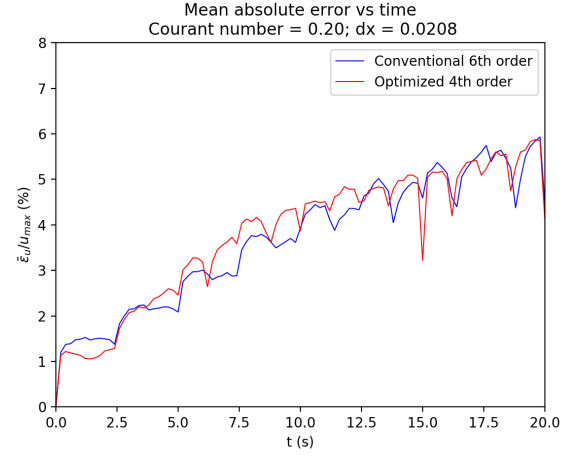
time. Absolute misfit between the numerically propagated wavefields and analytic solution (ϵ_u) was evaluated at each grid point, with the mean calculated for each scheme (see figure 3). Mean error was selected over maximum, as small phase differences were capable of producing large maximum errors, failing to reflect overall simulation quality.

To further investigate, $\frac{\bar{\epsilon}_u}{u_{max}}$ over time was plotted for each Δx . To avoid impractical runtimes, error was evaluated not at timesteps, but 0.2s intervals. Error plots over the region of interest are illustrated in figure 4.

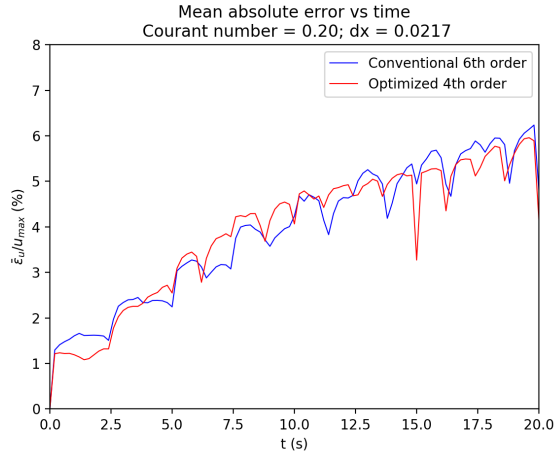
Examining wavefield evolution at $\Delta x = 0.0227m$ (the apparent crossover point in figure 4), nature of error in the two solutions appears to differ, despite being of comparable magnitude. For the conventional solution, high-frequency components exhibit phase shifts and distortion, apparent in figure 5b, particularly on “flat” sections of the wave. In contrast, error in the spatially-optimized solution appears to originate at steep gradients, generating slight misfit and spurious high frequencies which propagate outwards. This implies differing main error sources at this Δx , potentially explaining the discrepancy



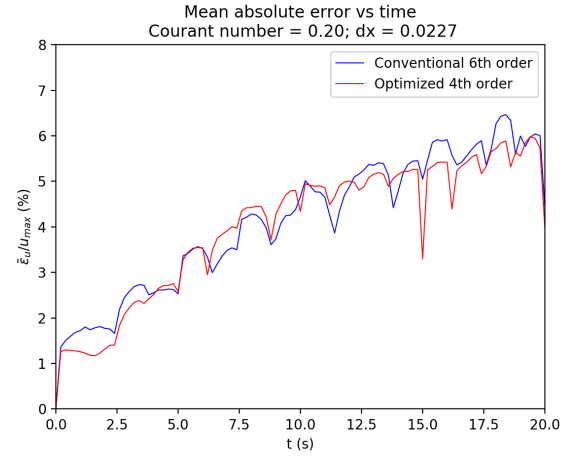
(a)



(b)



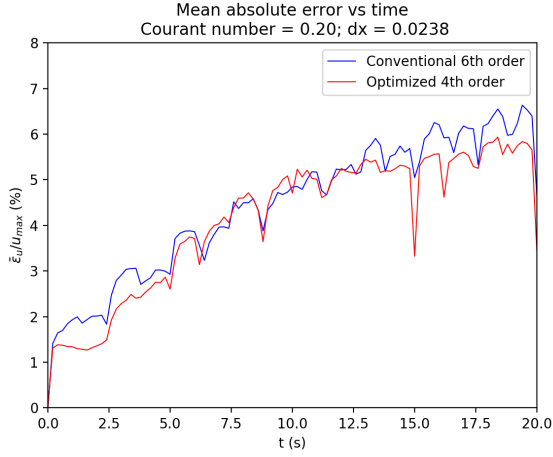
(c)



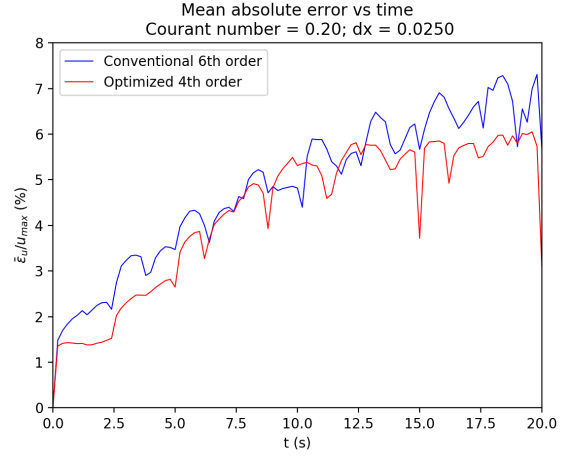
(d)

Figure (4) $\frac{\bar{\epsilon}_u}{u_{max}}$ versus time for various Δx . (Figure continued overleaf.)

between predicted convergence at $\Delta x \leq 0.0213\text{m}$ and actual at approximately $\Delta x \leq 0.0227\text{m}$.



(e)



(f)

Figure (4) $\frac{\bar{\epsilon}_u}{u_{max}}$ versus time for various Δx . Note the periodic dips in error coinciding with half the period of the standing wave, explaining the increased upper values of error when compared to figure 3. The optimized scheme is clearly superior when sampling is coarse. Over the course of a simulation using $\Delta x = 0.0250\text{m}$, the optimized scheme better fits the analytic solution at 64.0% of sampled timesteps, and 51.8% for $\Delta x = 0.0238\text{m}$, in agreement with figure 3. Convergence of the schemes as Δx is reduced is strongly apparent: both error-time curves trace similar paths in figures 4c and 4d. For $\Delta x = 0.0217\text{m}$ and $\Delta x = 0.0227\text{m}$, the optimized scheme is more accurate at 23.5% and 41.9% of sampled timesteps respectively, implying the performance crossover of the optimized 4th order and conventional 6th order schemes occurs at larger Δx than implied by figure 2. For $\Delta x = 0.0200\text{m}$ and $\Delta x = 0.0208\text{m}$ (figures 4a and 4b respectively), the optimized scheme produces the larger error, in agreement with predictions of behavior in this region, although implying that errors at 20s (see figure 3) are misleading and do not accurately represent overall propagation quality. This is affirmed by the optimized scheme having the smaller error at 8.6% and 11.4% of sampled timesteps for $\Delta x = 0.0200\text{m}$ and $\Delta x = 0.0208\text{m}$ respectively.

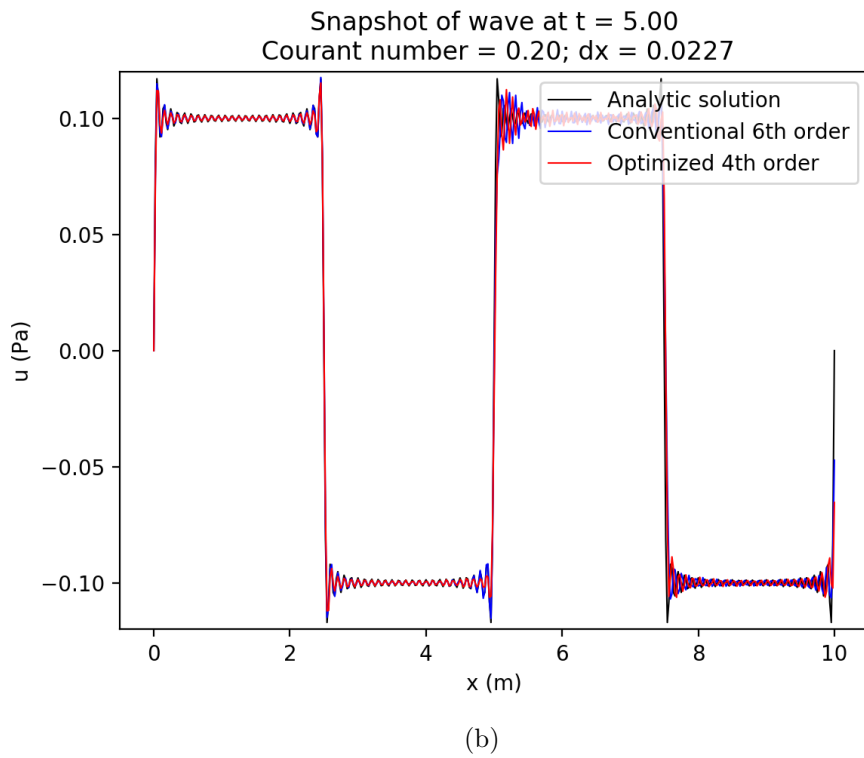
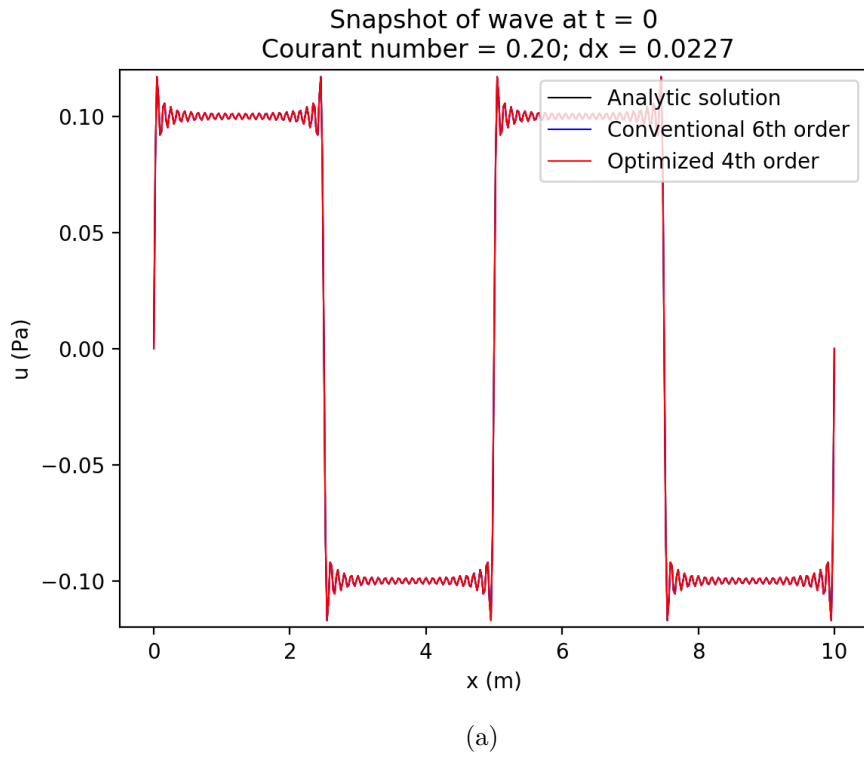
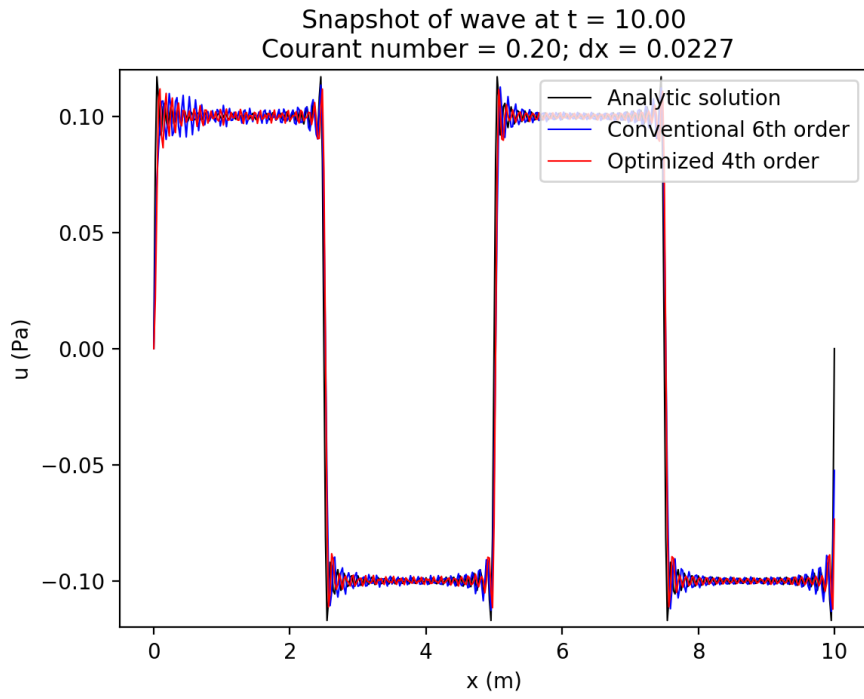
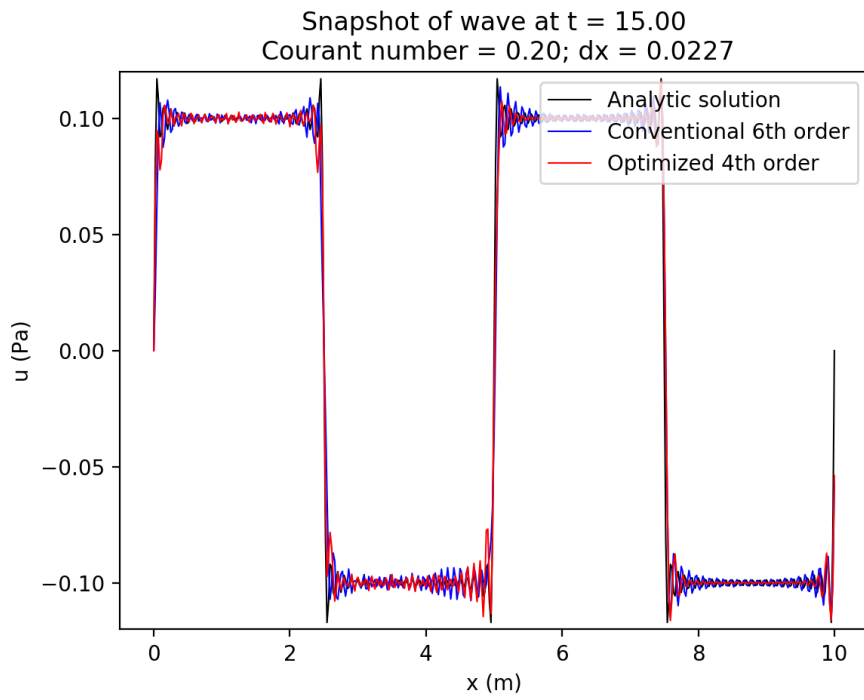


Figure (5) (Figure continued overleaf.)



(c)



(d)

Figure (5) (Figure continued overleaf.)

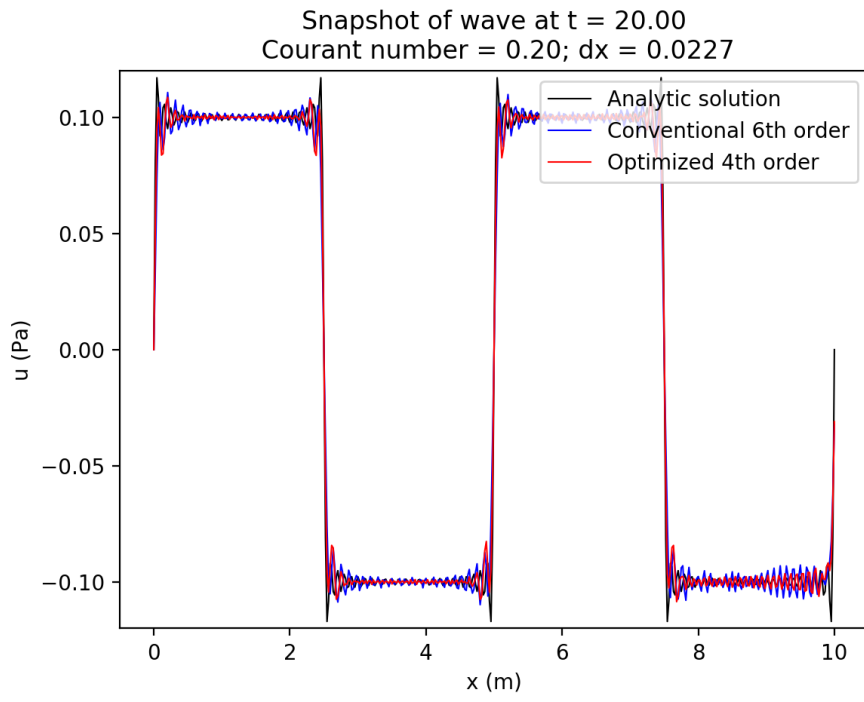


Figure (5) Evolution of the analytical, spatially-optimized FD, and conventional FD solutions at 5s intervals for $\Delta x = 0.0227\text{m}$.

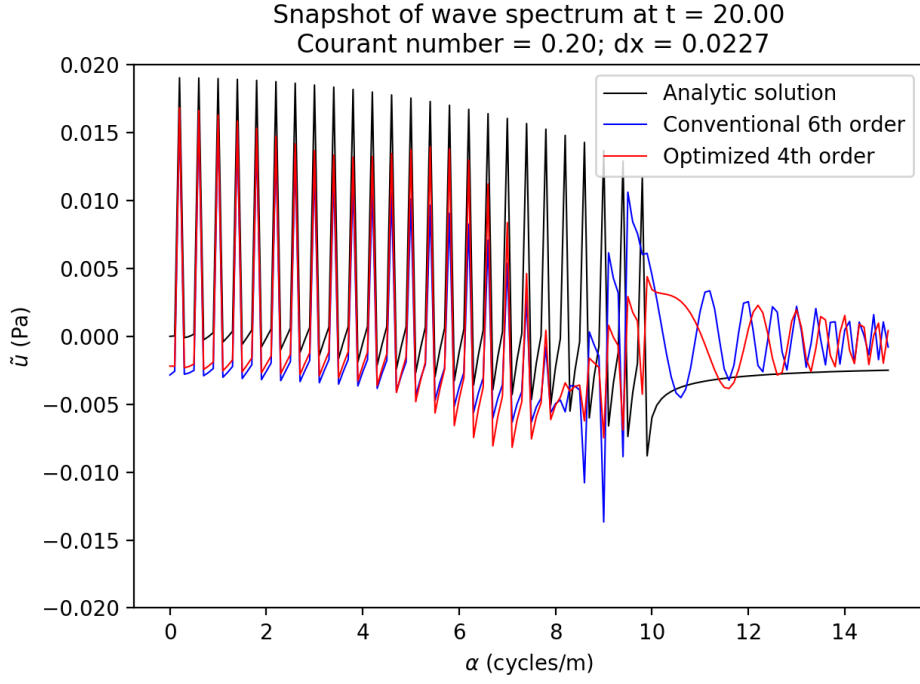


Figure (6) Spatial frequency amplitude spectrum of the analytical, spatially-optimized FD, and conventional FD solutions at 20s for $\Delta x = 0.0227\text{m}$. The normalized fast Fourier transform of the wavefield reveals significant distortion and phase shifts in the conventional FD solution, with considerable offset and some high-frequency components near polarity reversed. Whilst the optimized solution deviates from the exact spectrum in this region, the magnitude of misfit is reduced. Induced high frequencies are of approximately equivalent amplitude for both schemes, although they are present in different bands, becoming closer spaced at higher frequencies for both schemes. Overall spectral misfit is slightly greater for the conventional scheme, despite similar misfit in space.

3.4 General performance trends

For grid spacings where both schemes are subject to numerical dispersion, the 4th order optimized scheme should achieve greater accuracy than the 6th order conventional scheme; deviation from the ideal at the inflection point is smaller (see figure 2). For small Δx , wavefield sampling becomes saturated minimizing or eliminating numerical dispersion. In this circumstance, the 6th order conventional scheme should yield more accurate results as net error for both conventional and optimized schemes will be dominated by truncation error.

To verify, the test case was repeated over a wider range of grid spacings between $\Delta x = 0.0100\text{m}$ and $\Delta x = 0.0400\text{m}$, chosen to over and undersample the wavefield at respective extremes. The Δx interval was widened to coincide with the addition of 50 grid points to the computational domain, as smaller intervals were deemed prohibitively time consuming.

Error at simulation end versus Δx is shown in figure 7.

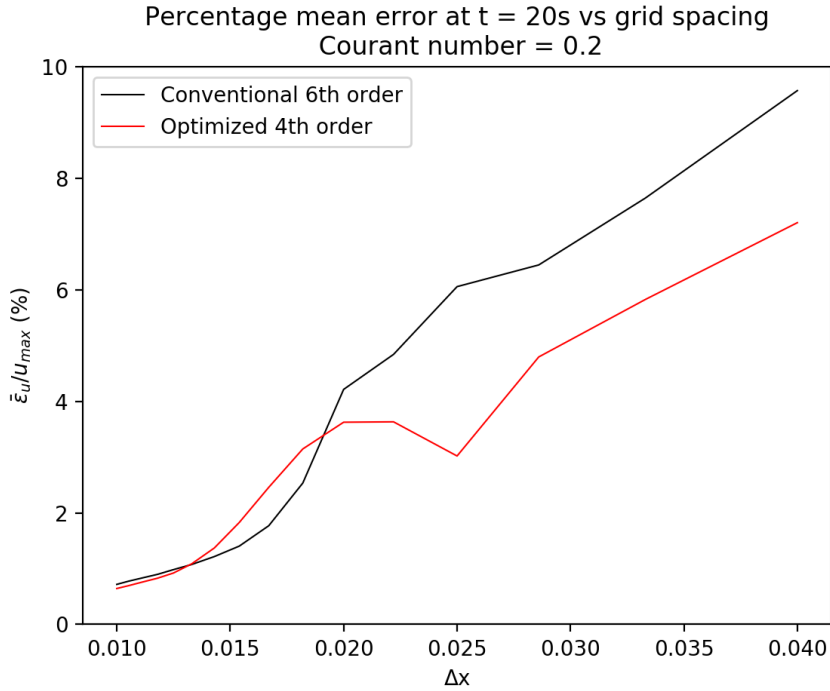


Figure (7) Mean absolute error ($\bar{\epsilon}_u$) evaluated at $t = 20\text{s}$ normalized against maximum amplitude over a wide range of Δx . This confirms that the optimized scheme offers considerable simulation quality improvements for undersampled wavefields, with $\frac{\bar{\epsilon}_u}{u_{max}} = 7.2\%$ versus $\frac{\bar{\epsilon}_u}{u_{max}} = 9.6\%$ for the conventional scheme at $\Delta x = 0.0400\text{m}$. However, overall performance difference between the two schemes is fairly rough when determined by this metric. Lower error in the optimized scheme for coarse grids corresponds with its reduced deviation from ideal dispersion characteristics for short wavelengths shown in figure 2. Error magnitude is considerably greater for both schemes when the wavefield is spatially undersampled due to dependence of truncation error on grid spacing. For moderately over-sampled wavefields, the conventional FD solution contains reduced error at simulation end, matching expected behavior as minimal numerical dispersion is eclipsed by truncation error. However, for very small Δx , the two schemes exhibit similar error with marginally less error in the optimized FD solution, implying that either the optimized scheme performs better than expected, or the conventional scheme experiences some undetermined drawback when both are applied to fine grids. The reduction of error in the optimized scheme between $\Delta x = 0.0200\text{m}$ and $\Delta x = 0.0250\text{m}$ apparent in figure 3 is present: the only decrease in error with increased Δx within the window studied. The mechanism behind this anomalous behavior is illuminated no further by the wider region of study, although it is of interest that it appears to cease at the maximum Δx required to avoid ambiguity in the wavefield.

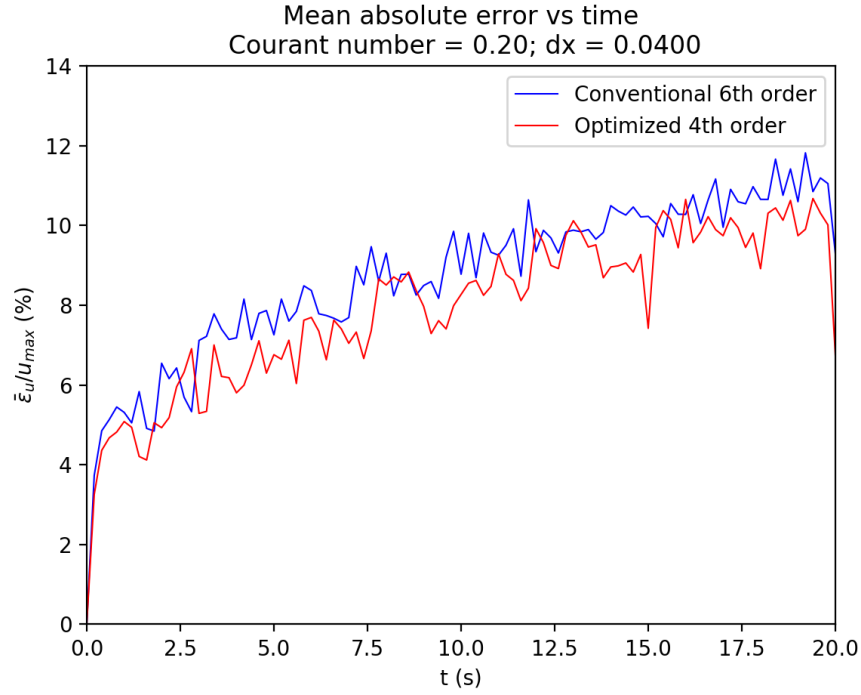
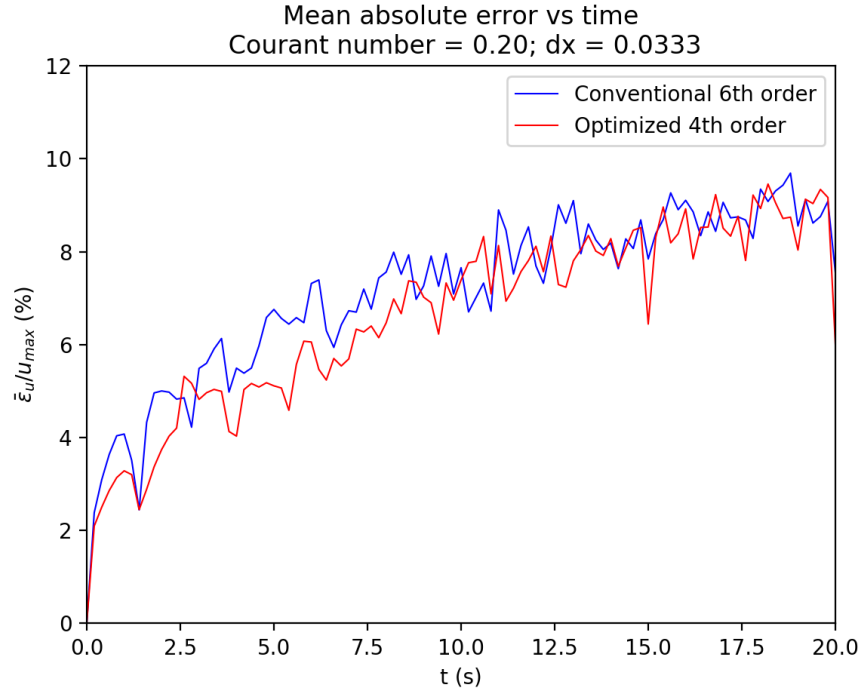


Figure (8) Evolution of mean absolute error over time for undersampled wavefields. It is apparent that the spatially-optimized scheme offers consistently better performance for undersampled wavefields, although perhaps not to the degree implied by figure 7. Errors in this plot are considerably larger than in figure 4, demonstrating that whilst spatial optimization has considerable benefits at large Δx , the waveform will still be distorted by undersampling.

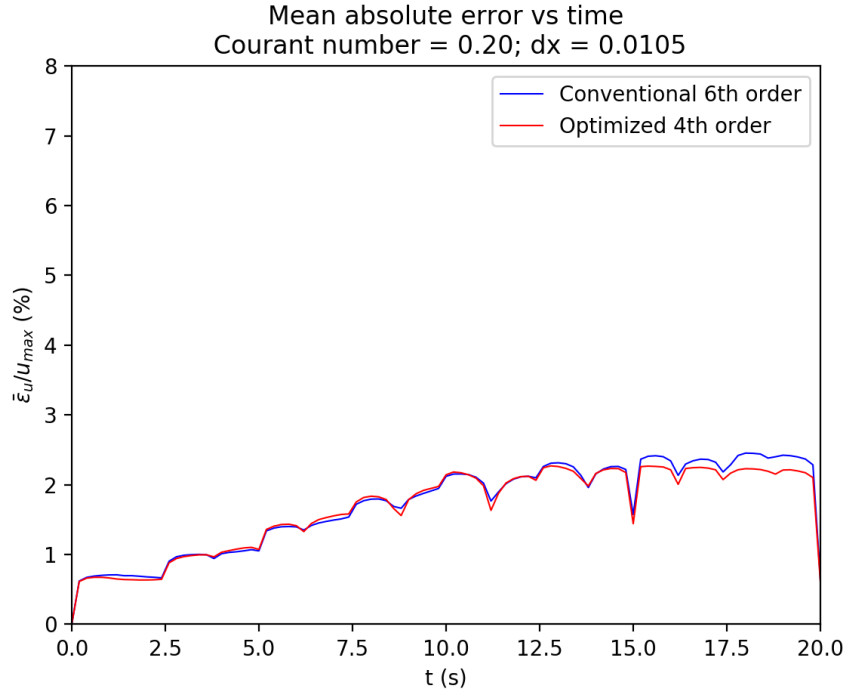
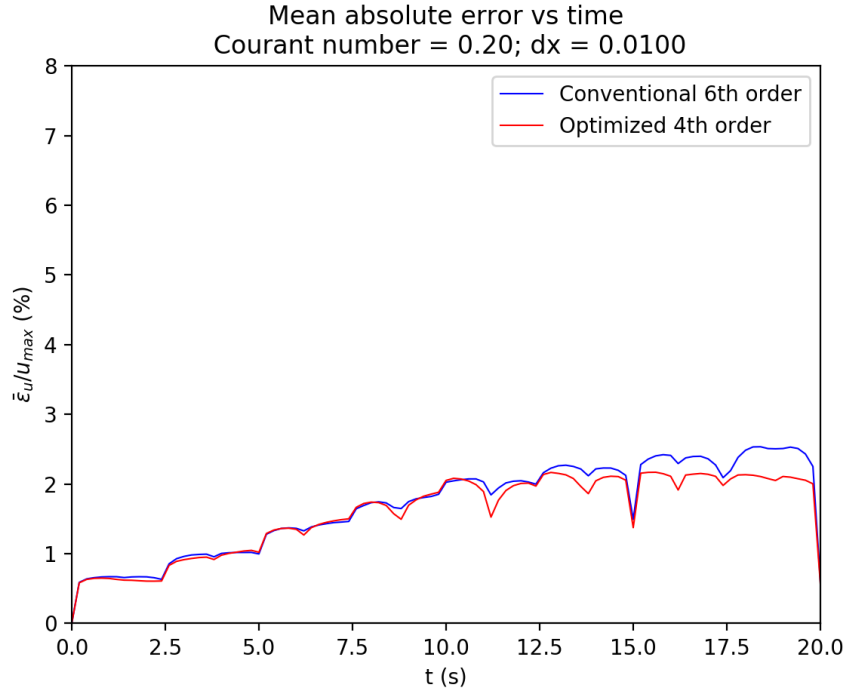


Figure (9) Evolution of mean absolute error over time for oversampled wavefields. Oversampled wavefields show minimal error generated by either scheme, with similar error up to approximately 10s, after which error in the optimized scheme does not appear to significantly increase. Error in the conventional scheme continues to accumulate after this point (albeit at a reduced rate), resulting in greater error for the conventional solution at simulation end. This contradicts expectations of superior performance for the conventional scheme at very small Δx , potentially implying some other error source inherent in conventional FD formulations. Note that error over time for the oversampled wavefields is considerably smoother than for the undersampled wavefields, possibly resulting from dependence of timestep size on Δx , leading to coarser temporal sampling when spatial sampling is coarse.

4 Test case: 2D elastic wave propagation

4.1 Model formulation

For seismic modeling, the elastic wave equation is often more useful than the acoustic wave equation, as both P and S waves are supported along with conversion between the two. As the elastic wave equation is a second-order, hyperbolic system, it is commonly substituted with a velocity-stress formulation based on the elastodynamic equations (e.g. Virieux, 1984, Virieux, 1986). Additionally, the second-order elastic wave equation suffers from issues arising from an unacceptable degree of dispersion in media with high values of Poisson's ratio (Bartolo et al., 2015, Stephen, 1988). The system can be expressed in terms of particle velocities and stresses to form a series of coupled equations, and is thereby transformed into the first-order, hyperbolic system

$$\begin{aligned}
\frac{\partial v_x}{\partial t} &= b \left(\frac{\partial \tau_{xx}}{\partial x} + \frac{\partial \tau_{xz}}{\partial z} \right) \\
\frac{\partial v_z}{\partial t} &= b \left(\frac{\partial \tau_{xz}}{\partial x} + \frac{\partial \tau_{zz}}{\partial z} \right) \\
\frac{\partial \tau_{xx}}{\partial t} &= (\lambda + 2\mu) \frac{\partial v_x}{\partial x} + \lambda \frac{\partial v_z}{\partial z} \\
\frac{\partial \tau_{zz}}{\partial t} &= (\lambda + 2\mu) \frac{\partial v_z}{\partial z} + \lambda \frac{\partial v_x}{\partial x} \\
\frac{\partial \tau_{xz}}{\partial t} &= \mu \left(\frac{\partial v_x}{\partial z} + \frac{\partial v_z}{\partial x} \right)
\end{aligned} \tag{23}$$

where (v_x, v_z) is particle velocity, τ_{xx} and τ_{zz} are normal stresses, and τ_{xz} is shear stress. First and second Lamé parameters are referred to as λ and μ respectively, and $b(x, z)$ is buoyancy: density's inverse.

To improve precision and stability, it is commonplace to use a staggered grid for elastic modeling applications (Liu and Sen, 2009a), evaluating derivatives on grids offset by $\frac{\Delta x}{2}$ from the reference grid. Velocity components are discretized on staggered grids with shear stress discretized at a staggered node to normal stresses in accordance with Virieux, 1986. Use of non-staggered grids with the P-SV formulation produces artifacts of similar amplitude to the data, and is thus inadvisable.

To prove the efficacy of spatially-optimized stencils for seismic modeling applications, optimized first derivative stencils for staggered grids have been derived for this system. To test feasibility of the method in practical applications, a 2 layer model consisting of water overlying shale, evocative of offshore surveys, was used. A 2km by 2km computational domain with $\Delta x = \Delta z = 10\text{m}$, divided into two layers each 1km thick was used. Layers were defined in terms of P-wave velocity, S-wave velocity, and density, from which Lamé parameters were obtained. The upper water layer had a P-wave velocity of 1400ms^{-1} and a density of 1000kgm^{-3} . As fluids do not support shearing, S-wave velocity was 0ms^{-1} . The lower shale layer had a P-wave velocity of 4000ms^{-1} , S-wave velocity of 2400ms^{-1} and a density of 2600kgm^{-3} . These values were informed by measurements from Castagna et al., 1985, Hamilton and Hamilton, 1978, and Greenspan et al., 1959 to ensure results analogous to real-world phenomena. The source function was a Ricker wavelet with a peak frequency of 11.2Hz, coinciding with the theoretical maximum frequency which can be propagated accurately by both the conventional and optimized staggered schemes (see figure 10). Note that as this frequency choice was based on S-wave velocity, longer-wavelength P-waves should be subject to reduced dispersion (Moczo et al., 2000). This source was injected into both normal stress fields at a centered position, 750m from the top of the domain.

This position was chosen such that incidence of the wave upon the layer boundary occurred prior to reflections from domain boundaries. External boundaries were kept as free surfaces to simplify implementation. A Courant number of 0.47 was used in accordance with stability conditions specified in Virieux, 1986 and a P-wave velocity of 6000ms^{-1} : well in excess of the model maximum, ensuring a good-quality solution.

4.2 Derivation of stencil coefficients

The 4th order spatially-optimized staggered first derivative has two stencil variants, $M = 3$, $N = 2$ and $M = 2$, $N = 3$, referenced henceforth as types “A” and “B” respectively. The former evaluates a derivative offset by half a grid spacing in the positive direction, whilst the latter yields the derivative half a grid spacing in the negative direction. For these stencils, equation 2 becomes

$$\frac{\partial u}{\partial x} \approx \frac{1}{\Delta x} \sum_{j=-N}^M a_j u \left(x + \left(j - \frac{1}{2} \right) \Delta x \right) \quad (24)$$

and

$$\frac{\partial u}{\partial x} \approx \frac{1}{\Delta x} \sum_{j=-N}^M a_j u \left(x + \left(j + \frac{1}{2} \right) \Delta x \right) \quad (25)$$

respectively. Values of E are thus expressed as

$$E_A = \int_{-\frac{\pi}{2}}^{\frac{\pi}{2}} \left| i\kappa + \sum_{j=-N}^M a_j e^{i(j-\frac{1}{2})\kappa} \right|^2 d\kappa \quad (26)$$

and

$$E_B = \int_{-\frac{\pi}{2}}^{\frac{\pi}{2}} \left| i\kappa + \sum_{j=-N}^M a_j e^{i(j+\frac{1}{2})\kappa} \right|^2 d\kappa \quad (27)$$

Coefficients of the type “A” stencil are constrained by

$$\begin{aligned} a_0 &= -a_1 \\ a_2 &= -a_{-1} = \frac{25}{48} - \frac{a_1}{2} \\ a_3 &= -a_{-2} = \frac{a_1}{10} - \frac{9}{80} \end{aligned} \quad (28)$$

whilst constraints for the type “B” stencil are

$$a_{-1} = -a_0$$

$$a_1 = -a_{-2} = \frac{25}{48} - \frac{a_0}{2} \quad (29)$$

$$a_2 = -a_{-3} = \frac{a_0}{10} - \frac{9}{80}$$

When minimization is carried out for the two stencils, the coefficients

$$a_0 = -a_1 = -1.1890097$$

$$a_2 = -a_{-1} = -0.07367152 \quad (30)$$

$$a_3 = -a_{-2} = 0.00640097$$

and

$$a_{-1} = -a_0 = -1.1890097$$

$$a_1 = -a_{-2} = -0.07367152 \quad (31)$$

$$a_2 = -a_{-3} = 0.00640097$$

are obtained for stencils “A” and “B” respectively. Note that these two stencils have identical coefficients shifted by a single grid point. Consequentially, both stencils are assumed to have identical dispersion characteristics.

Dispersion curves for conventional 6th order staggered and spatially-optimized 4th order staggered schemes are shown in figure 10.

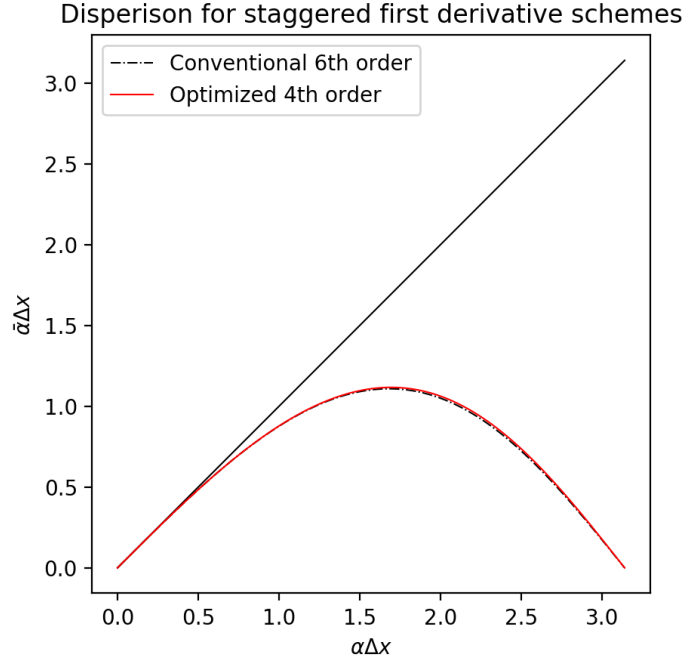


Figure (10) $\bar{\alpha}\Delta x$ versus $\alpha\Delta x$ for the conventional 6th order staggered and spatially-optimized 4th order staggered central-difference scheme. Note the only marginally better performance of the optimized scheme in terms of dispersion-relation-preservation. This is unsurprising, as the two have near-identical coefficients; the staggered conventional scheme is approximately optimized. Interestingly, both schemes deviate from the ideal at relatively small values of $\alpha\Delta x$ compared to second derivative schemes shown in figure 2. The conventional and optimized staggered schemes both require highest-frequency component wavelengths above $12.6\Delta x$. For shorter wavelengths, the optimized scheme will slightly better approximate propagation characteristics of a wave.

4.3 Performance at near-maximum grid spacings

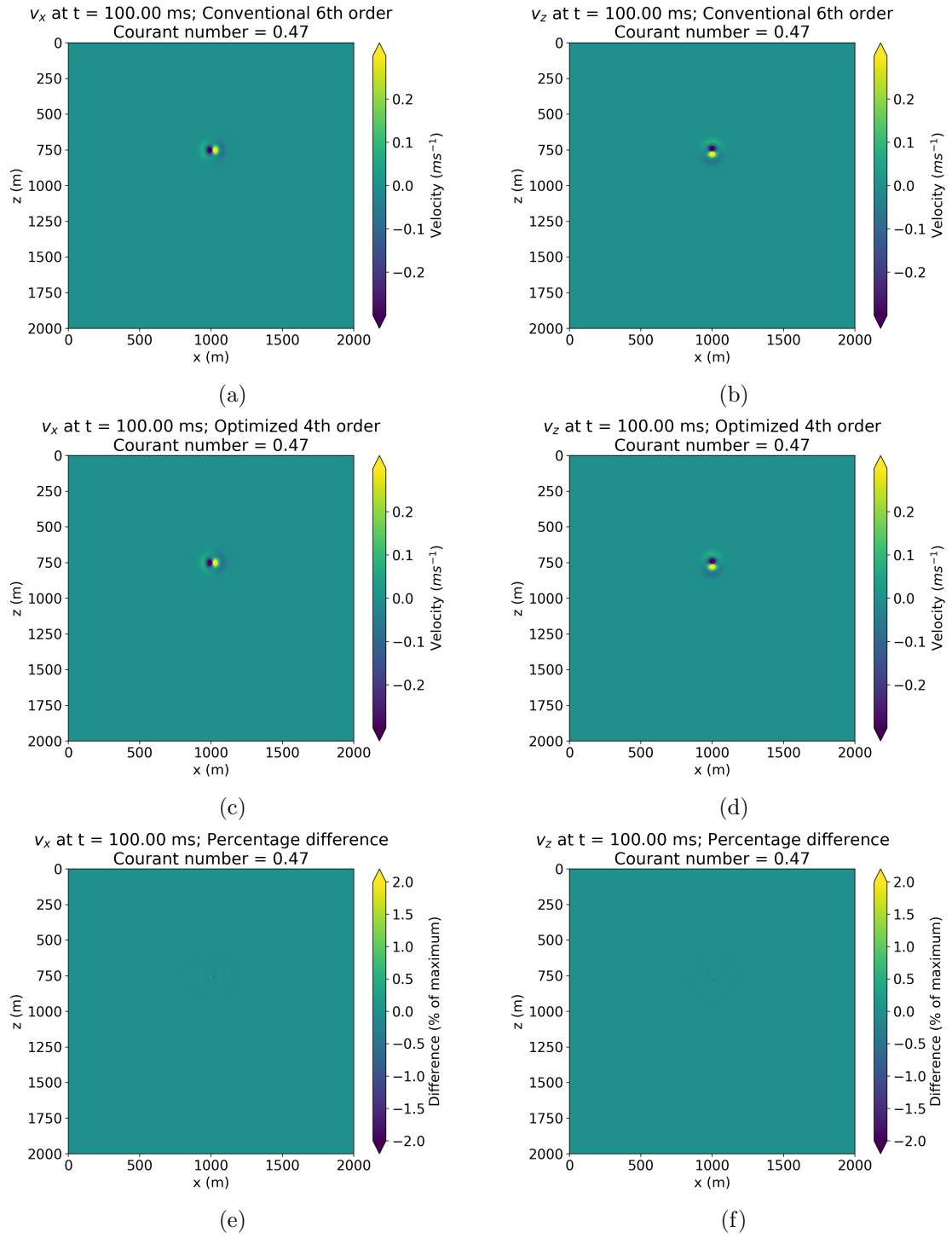


Figure (11) Wavefields for velocity components v_x and v_z calculated using conventional and optimized schemes at 100ms. Difference is normalized against the largest amplitude present in the wavefield.

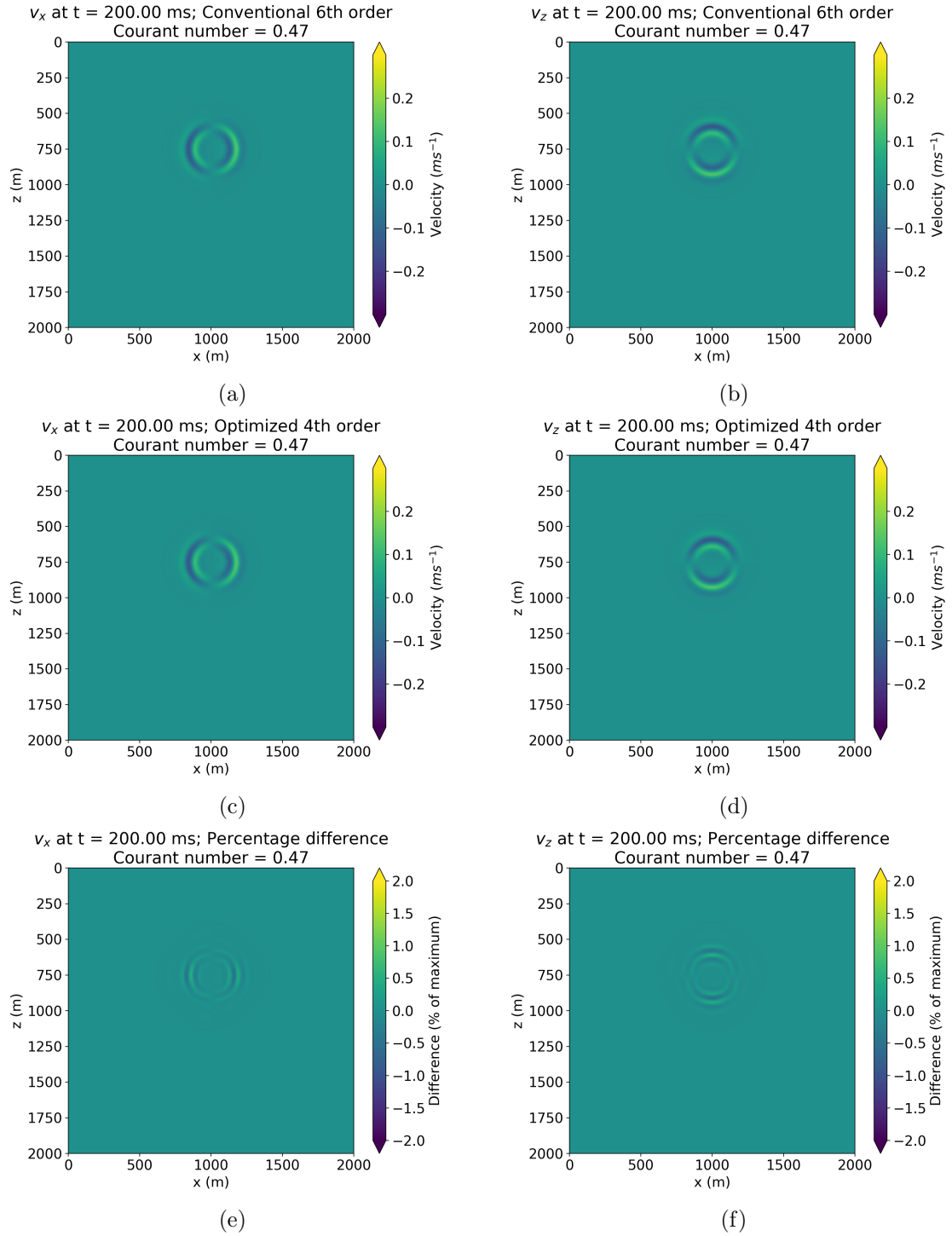


Figure (12) Wavefields for velocity components v_x and v_z calculated using conventional and optimized schemes at 200ms. Difference is normalized against the largest amplitude present in the wavefield.

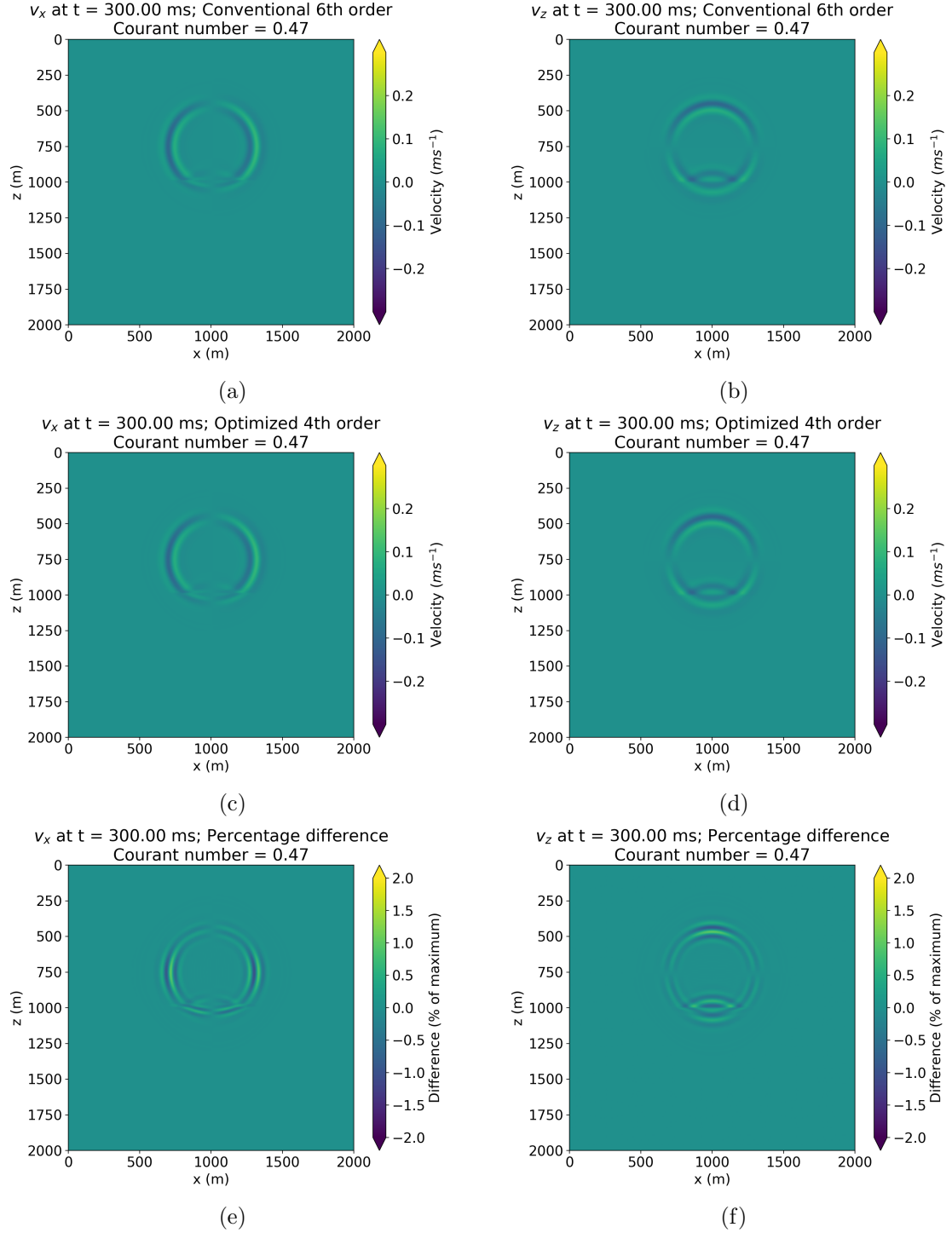


Figure (13) Wavefields for velocity components v_x and v_z calculated using conventional and optimized schemes at 300ms. Difference is normalized against the largest amplitude present in the wavefield.

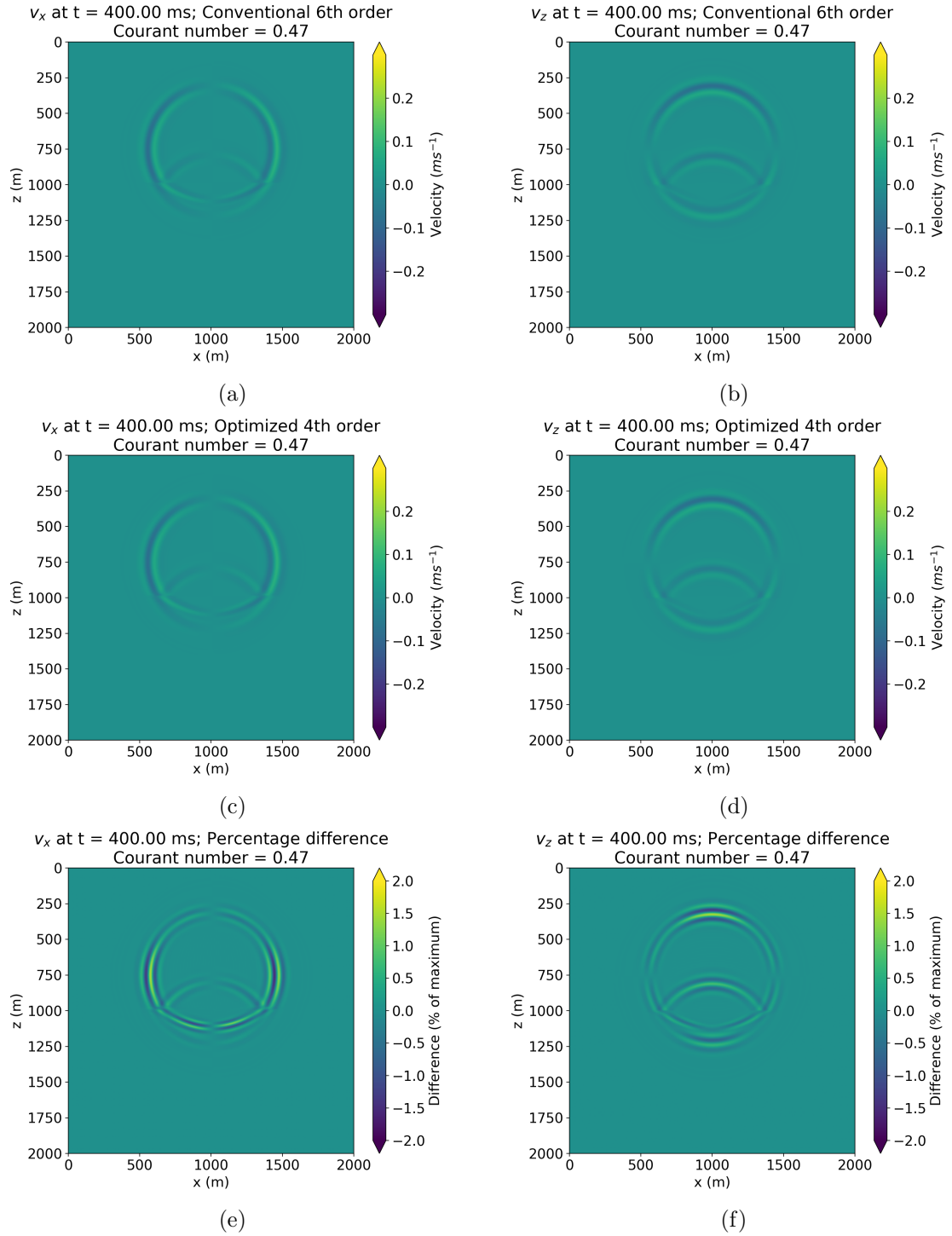


Figure (14) Wavefields for velocity components v_x and v_z calculated using conventional and optimized schemes at 400ms. Difference is normalized against the largest amplitude present in the wavefield.

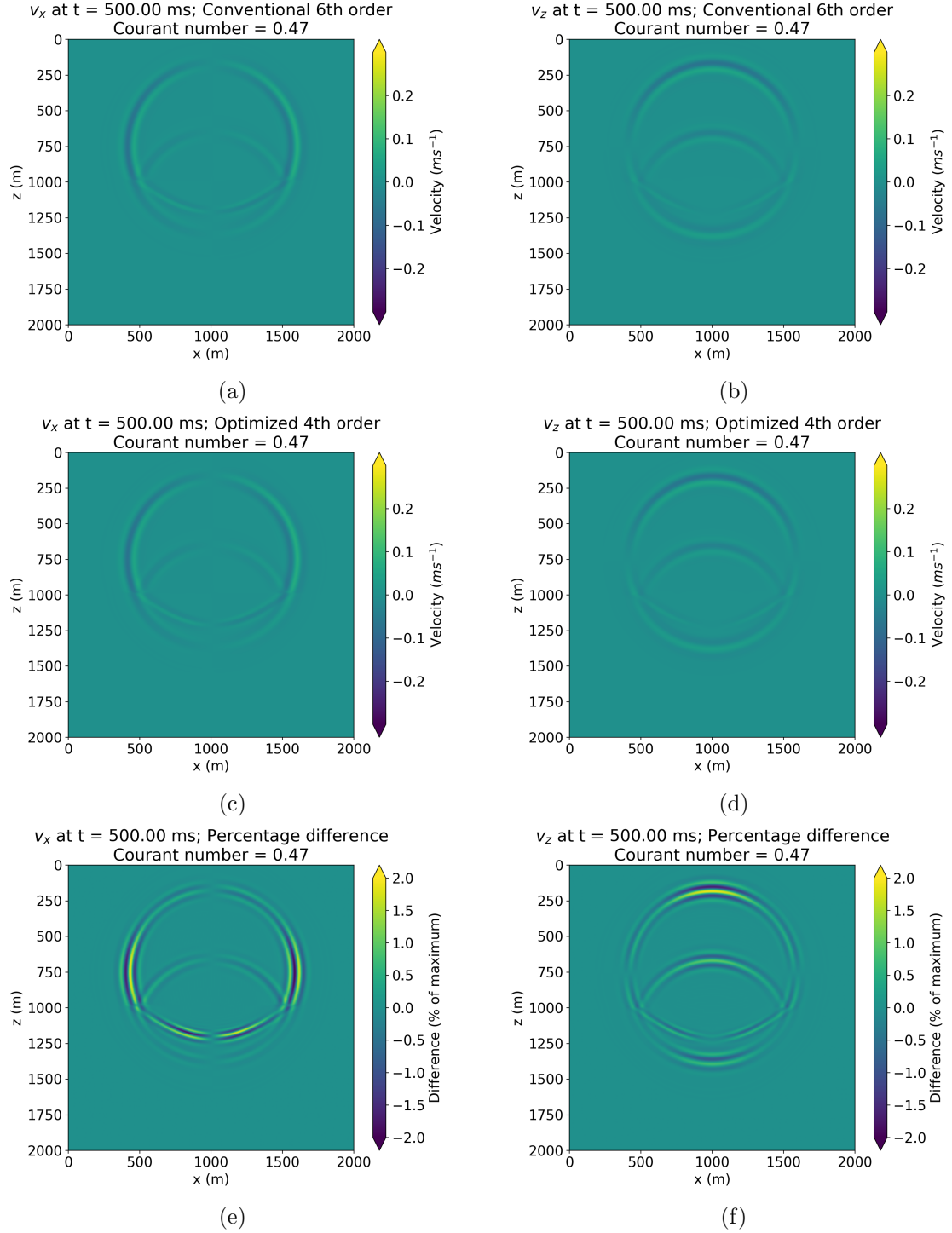


Figure (15) Wavefields for velocity components v_x and v_z calculated using conventional and optimized schemes at 500ms. Difference is normalized against the largest amplitude present in the wavefield.

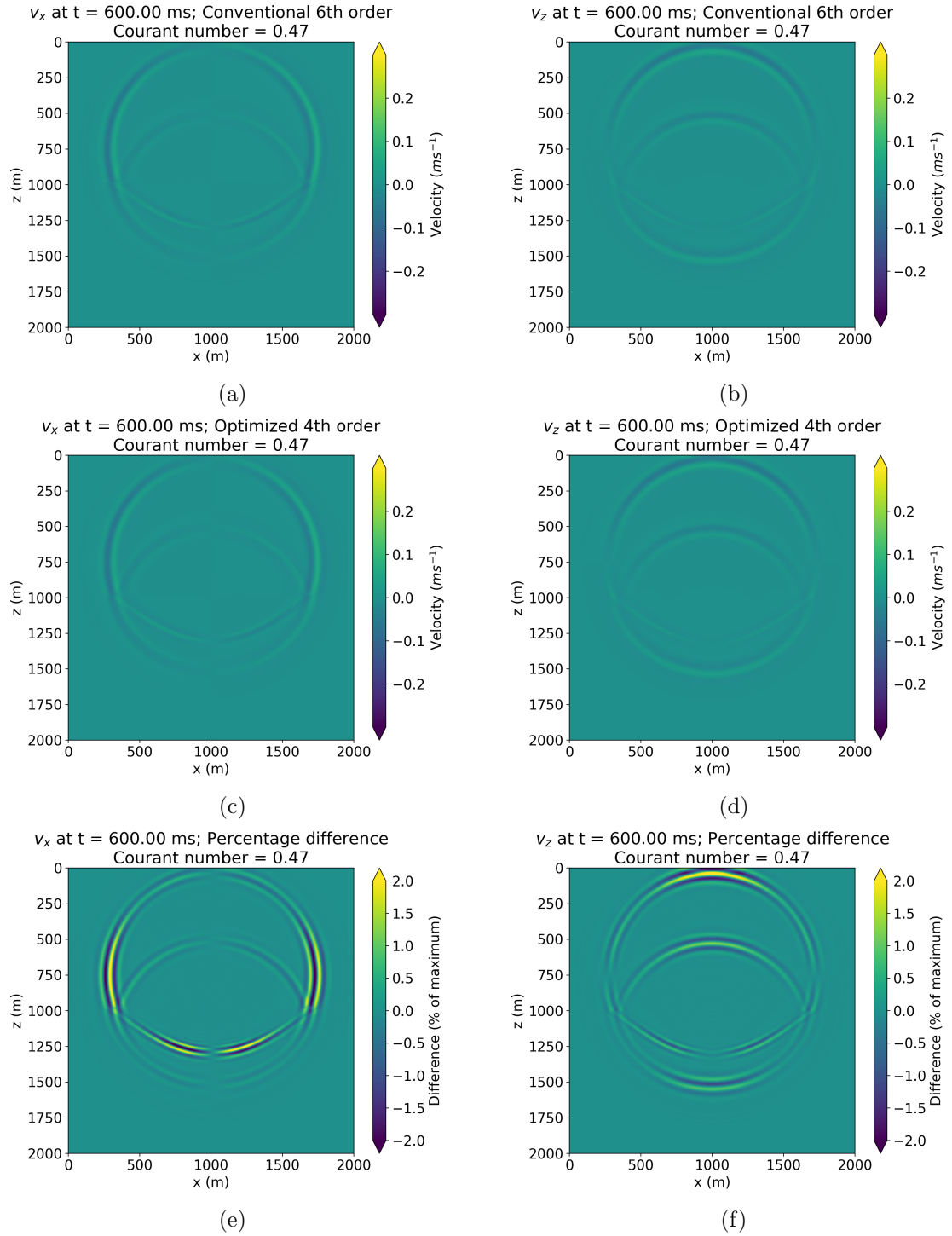


Figure (16) Wavefields for velocity components v_x and v_z calculated using conventional and optimized schemes at 600ms. Difference is normalized against the largest amplitude present in the wavefield.

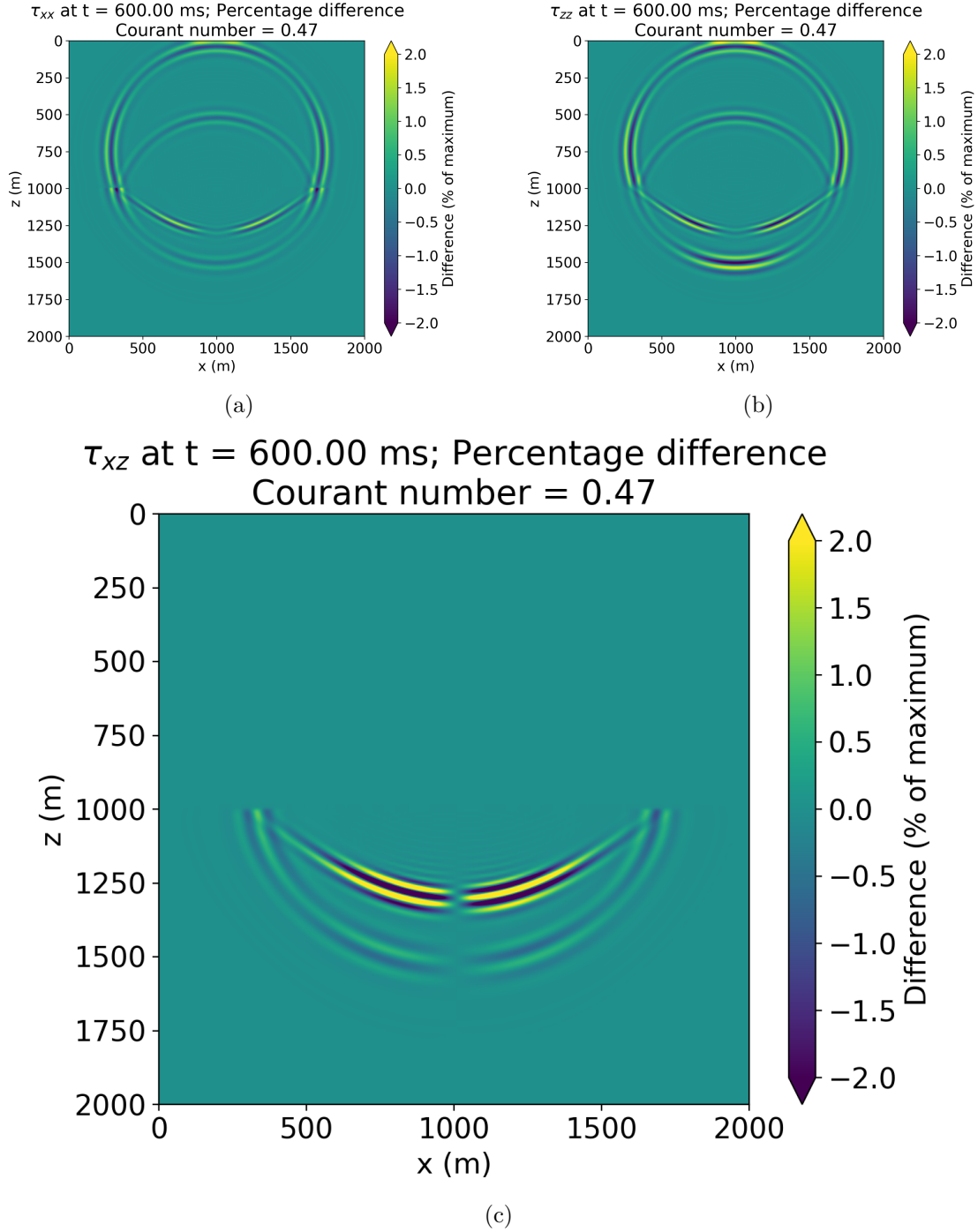


Figure (17) Difference between stress component wavefields for conventional and optimized schemes at 600ms (post-incidence on the shale layer), normalized against the largest amplitude present in the wavefield. S-waves are typically subject to increased numerical dispersion, as lower propagation speeds correspond with shorter wavelengths, thus coarsening wave sampling (Moczo et al., 2000). Figure 17 shows the highest-amplitude artifacts removed by the optimized scheme present in the τ_{xz} field, consistent with expectation. Artifact extent is also greatest in the τ_{xz} field, with trains of high-frequency ripples trailing behind the shear wavefront. Increased dispersion in the shear stress field is liable to induce inaccuracies in other fields if left to propagate, due to the coupled nature of stress and velocity for P-SV formulations.

Particle velocity components v_x and v_z over time are shown in figures 11 through 16. Little difference is discernible between the schemes at any time: not unexpected as both have similar stencil coefficients, producing near-identical dispersion characteristics. However, normalized difference between the wavefields for each scheme reveals a ring shaped artifact with wavelength half that of the main wavefront, and amplitude between 1% and 2% of the maximum amplitude. This artifact appears in the same position as the main body of the wave at all times. Upon inspection, this artifact appears squared, diagnostic of numerical dispersion (Juntunen and Tsiboukis, 2000), and extends inwards from the wavefront, characteristic of lagging high frequencies. Thus difference between the conventional and optimized FD solutions presumably consists primarily of numerical dispersion artifacts. The magnitude of the difference between fields generated by the conventional and numerical schemes is generally in agreement with differences in the expected degree of numerical dispersion suppression provided by each.

Both stencils generate satisfactory results for this model, thereby validating use of staggered spatially-optimized stencils for elastic wave propagation.

5 Discussion

5.1 Summary of test cases

For both test cases, the use of spatially-optimized 4th order stencils in the place of conventional 6th order yields notable improvements to simulation quality for Δx near or below the critical value for dispersion relation preservation, including for heavily undersampled wavefields. However, reduced truncation error in the higher-order conventional scheme results in better approximation of the governing PDE for finer grids, as the highest frequency wavefield components are sufficiently sampled to retain their dispersion characteristics. Note that whilst the optimized scheme yielded the smaller error at very small Δx for the first test case, this likely arose due to the parameters or nature of the test case in absence of a robust explanation.

Upon return to initial or reversed wave positions for the acoustic test case, the optimized solution tended to contain the smaller error, with smaller mean absolute error at simulation end for all Δx tested within the window $0.0200\text{m} \leq \Delta x \leq 0.0250\text{m}$. However, during transition between these states, misfit between the analytical and optimized FD solutions grows considerably. Whilst apparent in both schemes, the contrast appears more pronounced for the optimized scheme. This periodicity implies more accurate propagation of frequency components within the wave by the optimized scheme, minimizing distortion when the wave returns to its initial position. During the intermediate phase, the optimized scheme displays a tendency to generate high amplitude spikes adjacent to steep gradients which propagate with the position of these gradients. This should be noted when optimized schemes are used with models capable of producing steep gradients, as interpretation of these spurious spikes as meaningful data is liable to lead to inaccurate conclusions. This behavior could possibly be attributed to numerical coupling phenomena described by Tam and Webb, 1993, causing erroneous driving of frequency components when only the temporal or spatial stencils of a DRP scheme are used. In this case, use of the corresponding temporal derivative detailed in Tam and Webb, 1993 should address these artifacts.

Application of spatially-optimized stencils to staggered grids demonstrates viability of non-conventional FD stencils for elastic modeling. The optimized FD solution was found to be of similar quality to the conventional, although the difference between the two revealed limited increase in numerical dispersion in the conventional scheme. Otherwise, evolution of the wave was realistic and values observed in all fields were sensible for both schemes. The squared appearance of the dispersion artifact, with faces perpendicular to the x and z axis is consistent with maximum dispersion parallel with the x and z axis (Levander, 1988). This spurious directional dependence is apparent in orientations of the highest amplitude regions of the dispersion artifact, at left and right-most extremities for the v_x field, and top and bottom for v_z . The susceptibility of S-waves to numerical dispersion highlighted during testing

underlines the benefits of optimized schemes for multi-phase wavefields and dispersion-free handling of high-spatial-frequency waves originating from conversions at layer boundaries with reduced dispersion compared to conventional schemes. This implies more accurate propagation through complex models containing numerous layer boundaries, supported by findings in Zhang and Yao, 2013. The noteworthy reduction in numerical dispersion achieved demonstrates the transferability of the scheme’s DRP nature across multiple applications.

Despite considerable benefits of optimized schemes when applied to undersampled wavefields, the magnitude of error present was significantly greater than in adequately sampled wavefields. In the absence of computational constraints, use of high-order conventional FD schemes seems the obvious choice for numerically solving PDEs; fine grid spacings minimize the comparative benefits of optimized schemes with equivalent stencil extent. However, as memory constraints are commonplace in modeling applications, it is typically beneficial or even necessary to minimize the number of nodes within the computational domain. A smaller grid also ensures that simulation runtimes are not excessive, reducing the number of calculations per timestep. If the Courant number is held constant, then larger grid spacings yield larger timesteps, further reducing required calculation. If expediency is a priority, use of optimized schemes is preferable, not due to any inherent reduction in the number of computational operations, but because coarser spatial and temporal discretizations are possible.

For seismic applications, spatial optimization should typically be beneficial, despite only minimal improvement apparent in the second test case. Due to large memory requirements of the commonly used P-SV formulation (Virieux, 1986, Bartolo et al., 2015), the ability to run simulations at near critical Δx with marginal penalty is a boon. Combined with variable grid and time increments, this is exploitable to achieve an approximately 25% reduction in computational cost and memory demand (Zhang and Yao, 2013) without negatively impacting simulation quality. Note that as order increases, benefits of spatially optimizing a staggered scheme become increasingly pronounced (Liu, 2014). With the common requirement of accurate propagation over large distances necessitating good approximation of dispersion characteristics of the governing PDE, it is evident that optimized FD schemes should generally be chosen for seismic applications.

It is worth considering that seismic surveys are usually designed in accordance with available computational resources, such that high-frequency components liable to result in numerical dispersion during processing are excluded (Dablain, 1986). Thus in practice, spatial optimization may be unnecessary to ensure a good-quality solution in applications such as migration or forward modeling.

Note that extension to further spatial dimensions is straightforward for both standard and staggered grid formulations (Moczo et al., 2000). Beyond reduction of the formal accuracy order of the stencil, no clear disadvantages of spatial optimization were highlighted during testing.

5.2 Comparative performance and grid spacing

In the 1D acoustic test case, it was expected that error in both conventional and optimized schemes would be near-identical at the maximum grid spacing for acceptable propagation accuracy using the conventional scheme: $\Delta x = 0.0213$. The actual point of convergence was found to reside at an intermediate value between maximum grid spacings for the conventional and optimized schemes. This discrepancy resulted from interplay between truncation and numerical dispersion error.

Whilst studies have presented methods to quantify the truncation error in FD approximations (e.g. Lantz, 1971, Warming and Hyett, 1974), comparisons of dispersion and truncation error are scarce. Quantification of total error proportion contributed by each is thus difficult. Due to the tedious, time-consuming nature of existing error analysis methods (Warming and Hyett, 1974), error is typically determined empirically for some test case, evaluated relative to exact solutions or existing FD methods (e.g. Finkelstein and Kastner, 2007, Zhang and Yao, 2013). Additionally, whilst quantification of resolving power is commonplace in studies of DRP schemes (e.g. Tam and Webb, 1993, Liu, 2014),

these methods are not directly comparable with truncation error investigations, evaluating accuracy via different metrics.

Meaningful evaluation of respective contributions of dispersion and truncation error regarding the point of equal performance between the two schemes is consequentially near-impossible. However, test case results imply that conventional FD stencils should be considered when Δx is greater than the limit for good approximation of the dispersion relationship (so long as it is smaller than that for the optimized scheme). In practice, testing both schemes for Δx within these bounds and selecting the scheme which yields superior results is likely prudent. This approach is supported by the results of the 2D elastic test, demonstrating that for some problems, the optimized scheme will yield reduced error at maximum Δx for the conventional. Additionally, optimized schemes are found to achieve more accurate solutions under these circumstances in test cases described in Moczo et al., 2000 and Finkelstein and Kastner, 2007, supporting the notion that ideal scheme choice is somewhat dependent upon problem specification. Further investigation is required to develop a more robust understanding however.

5.3 Optimized scheme behavior for oversampled wavefields

The superior performance of the optimized scheme at very small values of Δx observed in the first test case is inconsistent with expectations based upon resolution characteristics and truncation error for the two schemes. At $\Delta x = 0.0100\text{m}$, sampling of the highest frequency component of the standing wave is well in excess of the number of grid spacings per wavelength required for preservation of propagation characteristics, producing minimal numerical dispersion for either scheme. It follows that higher-order truncation of the conventional stencil should result in reduced error under these circumstances. However, errors observed for both schemes between the start of the simulation and 10s were near-identical, with a reduction in error accumulation rate after this point, making apparent another peculiar aspect of the observed behavior of the optimized scheme: error in the numerical solution appears not to increase after this point.

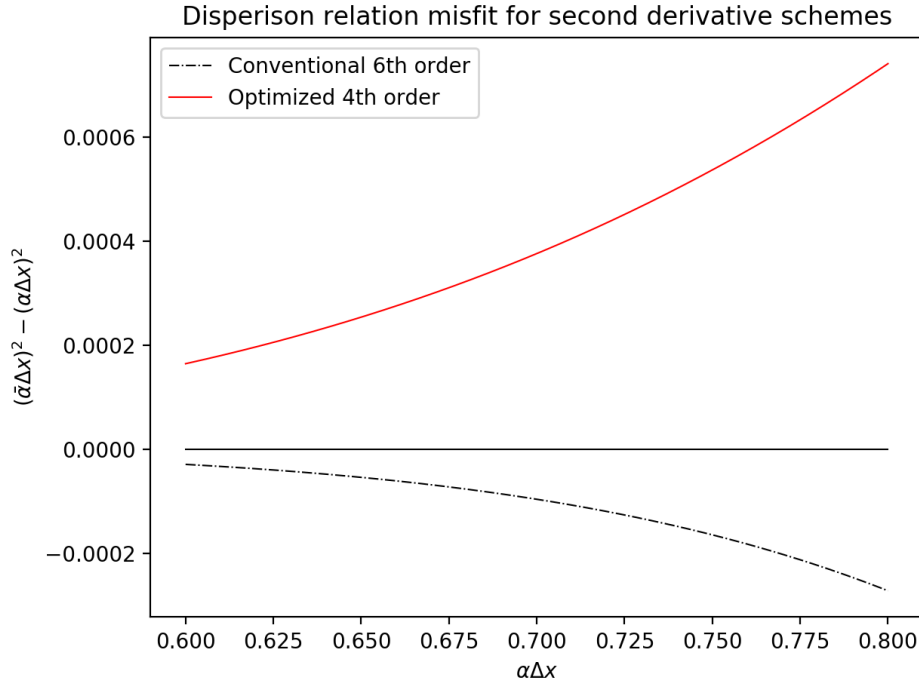


Figure (18) $(\bar{\alpha}\Delta x)^2 - (\alpha\Delta x)^2$ versus $\alpha\Delta x$ for the 4th order optimized and 6th order conventional central-difference schemes. The solid black line designates the ideal.

It is established that FD schemes will still produce some small degree of numerical dispersion, even for particularly fine grid spacings (Wang and Teixeira, 2003). Additionally, it has been demonstrated that DRP schemes can still marginally reduce numerical dispersion compared to conventional FD schemes for heavily oversampled wavefields (Wang and Teixeira, 2003). Considering the magnitude of the discrepancy between the two schemes observed in the 1D acoustic wave test case for small Δx , this presents a possible mechanism by which the optimized scheme could generate the smaller error. However, when the relationship between $\bar{\alpha}\Delta x$ and $\alpha\Delta x$ is examined against the ideal over the region of interest (see figure 18), it is clear that not only does the conventional scheme better approximate the second derivative, but the magnitude of misfit present is entirely inconsistent with that of the errors observed. Consequentially, it is unlikely that this is behind behavior exhibited by the first test case at small Δx .

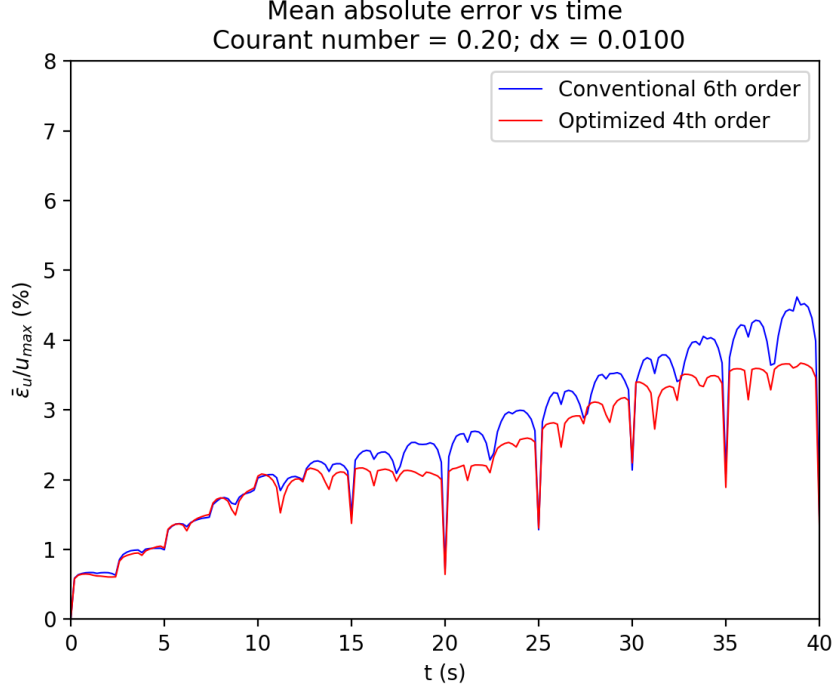


Figure (19) Evolution of mean absolute error over time for the 1D acoustic wave test case using $\Delta x = 0.0100\text{m}$. The simulation has been extended to $t=40\text{s}$. Note that the reduced rate of error introduction apparent in figure 9 is only temporary, and normal buildup of error resumes after 20s.

An alternative proposition is that the apparent reduction in the rate of change of error with time merely results from the chosen runtime, and expected behavior resumes at some later time outside the window studied. As the relation between mean error and time is fairly rough throughout, this is likely not an unreasonable assumption. To confirm, the first test case for $\Delta x = 0.0100$ was run to 40s as opposed to the 20s initially used. From the extended plot of mean absolute error against time in figure 19, it is clear that the apparent pause in error accumulation ends at approximately 20s. However, the unexplained superior performance of the optimized scheme continues until simulation end.

In the absence of a rigorous explanation for the superior performance of the optimized scheme for fine grid spacings, the observed behavior is assumed to result from some aspect of problem specification for the 1D acoustic test case. Similar behavior is reported for a comparable scheme in Tam et al., 1994, although its cause is not speculated on. Without further testing and error analysis of the FD schemes (e.g. Warming and Hyett, 1974), the cause of these observations remains unclear.

5.4 Limits to optimization benefits for staggered schemes

Dispersion characteristics of the conventional staggered scheme (see figure 10) are consistent with values published for comparable schemes in Saenger et al., 2000 and Moczo et al., 2000. Whilst the relationship between $\bar{\alpha}\Delta x$ and $\alpha\Delta x$ deviates from that of the underlying partial differential at a comparatively small value of approximately $\alpha\Delta x = 0.5$, it is apparent that the minimizations detailed in equations 26 and 27 yield little further improvement. The 6th order conventional staggered scheme for first derivatives can thus be considered near-optimized, posing the question as to whether this is inherent in staggered schemes, or merely coincidental.

The least-squares method of coefficient optimization for staggered grids detailed by Liu, 2014 yields identical coefficients to those derived for the 2D elastic test case. In assuming the equivalence of these methods, it follows that similarity between coefficients of the standard and optimized staggered schemes should extend only to stencils of small extent. As approximation order is increased, quality of the optimized FD solution differs increasingly from the conventional of equivalent stencil extent. The apparent limitations of spatial optimization for staggered grids in the derivation of stencils for the 2D elastic test case are therefore a product of stencil extent rather than an ubiquitous feature of staggered grid formulations. As high-order schemes are commonplace in seismic applications (e.g. Hong-wei et al., 2010), optimized schemes should typically offer considerable advantages over conventional stencils in practice.

6 Conclusions, evaluation, and further work

In this work, the spatial optimization method for developing DRP schemes proposed by Tam and Webb, 1993 has been extended for use with second derivatives and staggered grids. The optimized second derivative stencil was found to generate reduced error versus the conventional stencil of equivalent extent for wavefields with components of wavelength smaller than $4.4\Delta x$: somewhat larger than the theoretical value of $4.1\Delta x$. This discrepancy is postulated to result from the effects of truncation error. For lower frequency waves or finer grids, both schemes were capable of accurately resolving wave propagation characteristics, resulting in the conventional stencil yielding reduced error due to higher-order Taylor series truncation. However, for heavily oversampled wavefields, the optimized scheme was found to generate less error than the conventional. Whilst reports of this behavior exist in the literature, its causes remain unclear, although it is speculated to result from formulation of the test case or its parameters. It is proposed that notable error reduction at coarser grid spacings yielded by optimization be exploited to minimize computational cost, potentially augmented by variable temporal and spatial increments. This would yield considerable practical benefits in a suite of modeling applications.

The staggered optimized stencil for first derivatives was found to moderately improve numerical dispersion suppression versus the conventional stencil for wave components with wavelengths at the theoretical minimum for both schemes ($12.6\Delta x$). This was most pronounced in the τ_{xz} field, consistent with shorter wavelengths of slower S-wave components. Whilst optimized and conventional staggered stencils of 4th and 6th order respectively have similar coefficients and performance, benefits of spatial optimization are more pronounced for higher-order staggered stencils, implying suitability for seismic modeling and processing applications where high-order schemes are favored. Successful application of spatially-optimized schemes to the P-SV elastic wave formulation demonstrates viability of the method as a means of suppressing numerical dispersion in varied contexts. Consideration of spatially-optimized stencils is consequentially recommended for all applications featuring wavelengths near or below minimum values for accurate propagation.

Whilst the 1D example presented in the first test case is not dissimilar to several published examples, establishment of the method's validity benefited from a simple initial test case. Additionally, despite usage of spatially-optimized second-derivative stencils detailed in several publications, derivation of coefficients is rarely elaborated on. Whilst prevented by time and space constraints, further testing

with dispersive 1D examples may have aided better understanding of the level of numerical dispersion reduction offered by the optimized scheme, and the conditions under which it is most pronounced. The method detailed for spatial optimization of staggered grid stencils represents a considerably more straightforward means than existing methods, and has been demonstrated to provide tangible improvements when applied to simple seismic modeling applications. Without an exact solution, improvements in propagation accuracy for the optimized scheme are subject to a degree of uncertainty. However, as comparison to other FD schemes for performance evaluation is commonplace in published studies, this is unlikely cause for concern.

The derived spatially-optimized stencils would be complemented by temporal optimization to produce a full DRP scheme for staggered grid applications, further improving propagation accuracy of high-frequency components. It may also be of interest to investigate feasibility of stencil truncation upon accuracy of high-order optimized spatial derivatives, as this could potentially present means to considerably increase the accuracy of an FD scheme without additional computational cost. Viable avenues of inquiry also include integration of spatially-optimized FD methods into forward propagators for full-waveform inversion or migration algorithms, investigating potential benefits of increased propagation accuracy, or reduced runtime enabled by coarser grids.

References

- Bartolo, L. D., Dors, C., and Mansur, W. J. (2015). Theory of equivalent staggered-grid schemes : application to rotated and standard grids in anisotropic media. *Geophysical Prospecting*, 63(1):1097–1125.
- Castagna, P., Batzle, M. L., and Eastwood, R. L. (1985). Relationships between compressional-wave and shear-wave velocities in clastic silicate rocks. *Geophysics*, 50(4):571–581.
- Dablain, M. A. (1986). The application of high-order differencing to the scalar wave equation. *Geophysics*, 51(1):54–66.
- Etemadsaeed, L., Moczo, P., Kristek, J., Ansari, A., and Kristekova, M. (2016). A no-cost improved velocity-stress staggered-grid finite-difference scheme for modelling seismic wave propagation. *Geophysical Journal International*, 207(1):481–511.
- Fei, T. and Larner, K. (1995). Elimination of numerical dispersion in finite-difference modeling and migration by flux-corrected transport. *Geophysics*, 60(6):1830–1842.
- Finkelstein, B. and Kastner, R. (2007). Finite difference time domain dispersion reduction schemes. *Journal of Computational Physics*, 221(1):422–438.
- Greenspan, M., Tschiegg, C. E., and Tschiegg, C. E. (1959). Tables of the speed of sound in water. *Journal of the Acoustical Society of America*, 31(1):75–76.
- Hamilton, E. L. and Hamilton, L. (1978). Sound velocity-density rocks relations in sea-floor sediments and rocks. *Journal of the Acoustical Society of America*, 63(1):366–377.
- Hong-wei, L. I. U., Bo, L. I., Hong, L. I. U., Xiao-long, T., and Qin, L. I. U. (2010). The algorithm of high order finite difference pre-stack reverse time migration and GPU implementation. *Chinese Journal of Geophysics*, 53(4):600–610.
- Juntunen, J. S. and Tsiboukis, T. D. (2000). Reduction of Numerical Dispersion in FDTD Method Through Artificial Anisotropy. *IEEE Transactions on Microwave Theory and Techniques*, 48(4):582–588.
- Kim, I. and Hoefer, W. (1990). Numerical dispersion characteristics and stability factor for the TD-FD method. *IEEE Electronics Letters*, 26(7):485–487.
- Lantz, R. B. (1971). Quantitative Evaluation of Numerical Diffusion (Truncation Error). *Society of Petroleum Engineers Journal*, 251(2):315–320.
- Lele, S. K. (1992). Compact Finite Difference Schemes with Spectral-like resolution. *Journal of Computational Physics*, 42(103):16–42.
- Levander, A. R. (1988). Fourth-order finite-difference P-SV seismograms. *Geophysics*, 53(11):1425–1436.
- Liu, Y. (2009). Numerical modeling of wave equation by a truncated high-order finite-difference method. *Earthquake Science*, 22(2):205–213.
- Liu, Y. (2014). Optimal staggered-grid finite-difference schemes based on least-squares for wave equation modelling. *Geophysical Journal International*, 197(1):1033–1047.
- Liu, Y. and Sen, M. K. (2009a). A new time – space domain high-order finite-difference method for the acoustic wave equation. *Journal of Computational Physics*, 228(23):8779–8806.
- Liu, Y. and Sen, M. K. (2009b). A practical implicit finite-difference method : examples from seismic modelling. *Journal of Geophysics and Engineering*, 6(1):231–249.

- Luporini, F., Lange, M., Louboutin, M., Kukreja, N., Yount, C., Witte, P., Kelly, P. H. J., Uckelheim, J. A. N. H., Gorman, G. J., and Herrmann, F. J. (2018). Architecture and performance of devito, a system for automated stencil computation. *CoRR*, abs/1807.0:1–27.
- Madariaga, R. (1976). Dynamics of an expanding circular fault. *Bulletin of the Seismological Society of America*, 66(3):639–666.
- Moczo, P., Kristek, J., and Halada, L. (2000). 3D Fourth-Order Staggered-Grid Finite-Difference Schemes: Stability and Grid Dispersion. *Bulletin of the Seismological Society of America*, 90(3):587–603.
- Mufti, I. R., Pita, J. A., and Huntley, R. W. (1996). Finite-difference depth migration of exploration-scale 3D seismic data. *Geophysics*, 61(3):776–794.
- Saenger, E. H., Gold, N., and Shapiro, S. A. (2000). Modeling the propagation of elastic waves using a modified finite-difference grid. *Wave Motion*, 31(1):77–92.
- Stephen, R. A. (1988). A review of finite difference problems for seismo-acoustics at the seafloor. *Reviews of Geophysics*, 26(3):445–458.
- Tam, C. K. W., Shen, H., Kurbatskii, K. A., Auriault, L., Dong, Z., and Webb, J. C. (1994). Solutions of the benchmark problems by the dispersion-relation-preserving scheme. In *NASA conference publication 3300 ICASE / LaRC workshop on benchmark problems in conventional aeroacoustics*, number May 1995, pages 149–171.
- Tam, C. K. W. and Webb, J. C. (1993). Dispersion-relation-preserving finite difference schemes for computational acoustics. *Journal of Computational Physics*, 107(1):262–281.
- Tessmer, E. (2000). Seismic finite-difference modeling with spatially varying time steps. *Geophysics*, 65(4):1290–1293.
- Virieux, J. (1984). SH-wave propagation in heterogeneous media; velocity-stress finite-difference method. *Geophysics*, 49(11):1933–1957.
- Virieux, J. (1986). P-SV wave propagation in heterogeneous media: Velocity-stress finite-difference method. *Geophysics*, 51(4):889–901.
- Wang, S. and Teixeira, F. L. (2003). Dispersion-Relation-Preserving FDTD Algorithms for Large-Scale Three-Dimensional Problems. *IEEE Transactions on Antennas and Propagation*, 51(8):1818–1828.
- Wang, Y., Liang, W., Nashed, Z., Li, X., and Liang, G. (2014). Seismic modeling by optimizing regularized staggered-grid finite-difference operators using a time-space-domain dispersion-relationship-preserving method. *Geophysics*, 79(5):277–285.
- Warming, R. F. and Hyett, B. J. (1974). The Modified Equation Approach to the Stability and Accuracy Analysis of Finite-Difference Methods R. F. *Journal of Computational Physics*, 14(1):159–179.
- Whitham, G. (1974). *Linear and nonlinear waves*.
- Yan, H. and Liu, Y. (2013). Acoustic prestack reverse-time migration using the adaptive high-order finite-difference method in the time-space domain. *Chinese Journal of Geophysics*, 56(2):181–195.
- Yan, H., Liu, Y., and Zhang, H. (2013). Prestack reverse-time migration with a time-space domain adaptive high-order staggered-grid finite-difference method. *Exploration Geophysics*, 44(1):77–86.
- Yan, Z., Yang, L., and Zhi-ming, R. (2014). Viscoacoustic prestack reverse time migration based on the optimal time-space domain high-order finite-difference method. *Applied Geophysics*, 11(1):50–62.

- Yang, D., Song, G., Hua, B., and Calandra, H. (2010). Simulation of acoustic wavefields in heterogeneous media : A robust method for automatic suppression of numerical dispersion. *Geophysics*, 75(3):99–110.
- Yang, D., Teng, J., Zhang, Z., and Liu, E. (2003). A Nearly Analytic Discrete Method for Acoustic and Elastic Wave Equations in Anisotropic Media. *Bulletin of the Seismological Society of America*, 93(2):882–890.
- Zhang, J.-h. and Yao, Z.-x. (2013). Optimized finite-difference operator for broadband seismic wave modeling. *Geophysics*, 78(1):13–18.